Materials Today Bio 20 (2023) 100643

Contents lists available at ScienceDirect

Materials Today Bio

journal homepage: www.journals.elsevier.com/materials-today-bio

Albumin-based formononetin nanomedicines for lung injury and fibrosis therapy via blocking macrophage pyroptosis

Boshu Ouyang [a,b,1], Lingling Deng [a,b,1], Fangyong Yang [a,b], Hanlin Shi [a,b], Na Wang [a,b], Weifeng Tang [a,b], Xi Huang [a,b], Yaolong Zhou [a,b], Hang Yu [a,b], Ying Wei [a,b,**], Jingcheng Dong [a,b,*]

[a] Department of Integrative Medicine, Huashan Hospital, Fudan University, Shanghai, 200040, PR China
[b] Institutes of Integrative Medicine, Fudan University, Shanghai, 200040, PR China

ARTICLE INFO

Keywords:
Lung injury
Fibrosis
Macrophage pyroptosis
SPARC
Formononetin
NLRP3

ABSTRACT

Pulmonary fibrosis that occurs following lung injury is a progressive and fatal disease since continual damage to lung tissue triggers the dysregulated inflammation response and accompanying abnormal healing process. Pyroptosis of alveolar macrophages has been found to play an essential role in the deterioration of lung injury and fibrosis. However, the lack of inhibitors against this inflammatory cell death in macrophages and the dense stroma pose major barriers to lung injury and fibrosis treatment. Herein, we developed an albumin-based nanoformulation to realize active delivery of formononetin (FMN) to improve the treatment of lung injury and fibrosis. The obtained nanoparticle, FMN@BSA NPs, could efficiently accumulate at the impaired lesion benefiting from the leaky vasculatures and the affinity between albumin and the overexpressed SPARC protein. Through blocking the NLRP3 inflammasome-involved pyroptosis process of macrophages, FMN@BSA NPs remarkably improved lung function and prolonged animal survival in the bleomycin (BLM)-induced lung injury and fibrosis model without noticeable side effects. Meanwhile, we proved FMN as a pyroptosis inhibitor and the corresponding lipid metabolism-related mechanisms through multi-omics analysis. This study first employed an albumin-based nanoparticle to deliver the pyroptosis inhibitor to the impaired lung tissue actively, providing a promising strategy for lung injury and fibrosis treatment.

1. Introduction

Acute lung injury (ALI), caused by a variety of etiologies, ranging from physical damage and medication-mediated side effects to viral or bacterial infections like SARS-CoV-2, can initiate the dysregulated inflammatory reaction, leading to diffuse pulmonary edema and acute respiratory insufficiency [1,2]. Along with advanced ALI, pulmonary fibrosis (PF) develops since persistent damage to the alveolus triggers an abnormal healing process and progressive scarring in lung tissue, resulting in impaired lung function and eventual death [3]. Once PF occurs, apart from lung transplantation with a high risk of immune rejection, pirfenidone (PFD) and nintedanib serve as the only approved drugs for attenuating the extracellular matrix (ECM) deposition and preserving lung function. However, these drugs fail to significantly improve the prognosis of patients and achieve little clinical success due to their overall ineffectiveness [4,5]. Therefore, there is an urgent need for more effective therapeutics against lung injury and fibrosis.

The incompletely understood pathogenesis underlying lung injury and secondary fibrosis pose challenges in developing effective therapeutics for this fatal lung disease. As the most abundant immune effector cells involved in the host defense, alveolar macrophages play a vital role in balancing the inflammatory process and the subsequent damage repair [6]. Furthermore, accumulating evidence disclosed that the severe inflammation caused by macrophage death is positively related to the initiation and progression of scarring. Consistent with the elevated levels of caspase-1 and interleukin-1β (IL-1β) in bronchoalveolar lavage fluid (BALF) from ALI patients [7,8], several studies demonstrated that continual pathogenic conditions frequently propel these defensive cells

* Corresponding author. Department of Integrative Medicine, Huashan Hospital, Fudan University, Shanghai, 200040, PR China.
** Corresponding author. Department of Integrative Medicine, Huashan Hospital, Fudan University, Shanghai, 200040, PR China.
E-mail addresses: weiying_acup@126.com (Y. Wei), jcdong2004@126.com (J. Dong).
[1] Both authors contributed equally to this work.

https://doi.org/10.1016/j.mtbio.2023.100643
Received 3 January 2023; Received in revised form 23 March 2023; Accepted 23 April 2023
Available online 25 April 2023

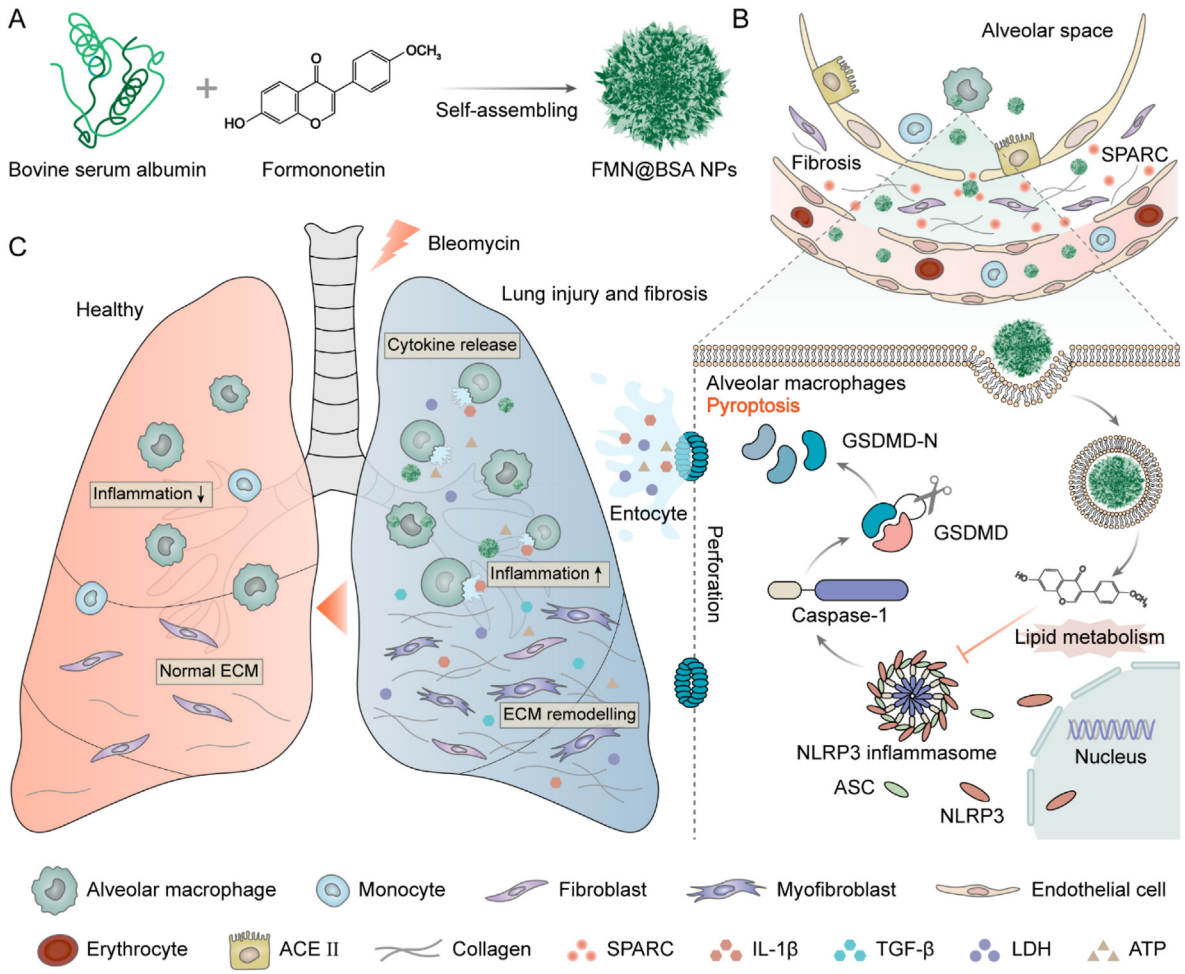

Scheme 1. Schematic illustration of FMN@BSA NPs for the treatment of lung injury and fibrosis. A) Construction of FMN@BSA NPs. B) Preferential accumulation of FMN@BSA NPs in the impaired lesion by taking advantage of the leaky interstitial lung vasculature and the high affinity between albumin and locally overexpressed SPARC. C) The therapeutic effects of FMN@BSA NPs on lung injury and fibrosis caused by pyroptosis inhibition on alveolar macrophages.

to undergo pyroptosis accompanied by the release of various pro-inflammatory cytokines, thereby amplifying the inflammation reaction and triggering the overactivation of fibroblasts [9,10]. Therefore, medications that block the pyroptosis of macrophages in the lung injury microenvironment could serve as a practical strategy to restore the defense-to-repair homeostasis and thus alleviate fibrosis.

Moreover, during the inflammation phase, the microcirculatory impairment produced by the disruption of endothelial cell barrier integrity in lung tissue leads to poor drug accessibility, representing additional challenges related to *in vivo* exerting therapeutic effects and even verifying mechanisms of action [11]. As for the fibrogenic stage, the ECM secreted after injury causes elevated interstitial fluid pressure, compressed vasculatures, and physical barriers, leading to a limited blood supply and impaired drug accumulation at the diseased site [12]. It is challenging for the commonly used free drugs to rapidly reach their effective concentrations in the lesion microenvironment, mainly through passive diffusion. As a result, targeted transportation of the therapeutics to the injured lesions by the rationally designed delivery systems might serve as a practical strategy for improving drug efficacy as well as reducing systemic toxicity [13,14].

Collectively, developing a pyroptosis inhibitor encapsulated in a tailored targeting formulation provides a feasible treatment regimen for the management of lung injury and fibrosis. According to the pyroptotic process in ALI, nucleotide-binding and oligomerization domain (NOD)-like receptor protein 3 (NLRP3), expressed predominately in macrophages, undergo activation and oligomerization stimulated by the pathological factors, which could further trigger the caspase-1-mediated cleavage of the perforator protein gasdermin D (GSDMD) [15–17]. Subsequently, the cleaved GSDMDs form transmembrane pores that release cellular contents and inflammatory factors, leading to aggravated local inflammation reactions and further fibrogenic response [9,18]. Thus, drugs that block NLRP3 of macrophages at the diseased site hold the potential to improve the treatments of lung injury and fibrosis by pyroptosis inhibition. As for the targeted delivery system, although the increased solid stress and insufficient blood supply caused by the damage-repair cascade of tissues impair drug distribution to injured sites, the compressed and leaky vasculatures are conducive to the extravasation of nano-sized agents [12]. From another perspective, the abundant extracellular proteins provide more targetable biomarkers for developing active targeting drug delivery systems, which could enhance drug retention through ligand-receptor-mediated interaction [11,19]. Secreted protein acidic and rich in cysteine (SPARC), a matricellular glycoprotein that promotes ECM deposition, is overexpressed in the wounded and remodeling microenvironment and showed a high affinity to endogenous albumin [20–22]. As a natural carrier of hydrophobic molecules in the blood, albumin has been maturely applied in the preparation of nanoparticles for various hydrophobic drugs [23–25]. In addition, the high inflammatory environment and the rapid metabolic capacity of fibrotic cells further enhance albumin uptake. Hence, besides more biocompatibility than synthetic ligands, an albumin-based nanoformulation might maximize the pathological characteristics of lung injury and fibrosis to realize the preferential accumulation of functional

agents by both passive extravasation and active binding.

Herein, we designed an albumin-based nanoparticle to actively deliver the pyroptosis inhibitor to injured lung tissue to relieve the inflammation reaction and further attenuate the stroma deposition. Formononetin (FMN), a natural product proven to significantly inhibit airway inflammation and remodeling by our previous work [26], was chosen to block pyroptosis in macrophages. FMN with ideal biosafety profiles has been reported to repress the NLRP3-related pathway in a range of inflammation diseases, but the strong hydrophobicity and poor stability compromise its *in vivo* applications [27,28]. Given the ability to load hydrophobic drugs, the albumin-based nanoparticle was prepared for FMN to facilitate its preferential accumulation and improve its bioavailability. Specifically, we first demonstrated FMN as a potential inhibitor to block NLRP3-involved inflammasome activation and further prevent pyroptosis in macrophages. Then, the FMN-containing bovine serum albumin nanoparticles, termed FMN@BSA NPs, were developed by the nanoprecipitation method (Scheme. 1). The obtained FMN@BSA NPs with favorable size were expected to protect FMN from clearance and extravasate from the abnormal vessels within the injured lesion. The strong binding affinity between albumin and SPARC protein could further promote the targeted accumulation and enhance the retention of the nanoparticles. Following internalization by macrophages, FMN would be rapidly released to suppress the assembly of NLPR3 inflammasomes, disrupt the pyroptosis process, and decrease the secretion of pro-inflammatory cytokines, thereby reducing the continuous inflammation reaction-mediated fibrogenic response.

As expected, FMN@BSA NPs efficiently accumulated at the impaired lesion, significantly inhibited pyroptosis in macrophages by blocking the NLRP3 inflammasome pathway, and finally attenuated immune response and stroma in the murine lung injury and fibrosis model. In this study, we first proved FMN as a pyroptosis inhibitor to alleviate lung injury progression and demonstrated the lipid metabolism-related mechanism through proteomics/metabolomics analysis. Moreover, we first adopted the albumin nanoparticle as an actively targeting carrier to efficiently deliver therapeutics to lung injury and fibrosis lesions. With the assistance of this delivery system, we verified the macrophage pyroptosis-involved pathological mechanisms of lung injury and fibrosis *in vivo* and *in vitro*. Collectively, our findings demonstrated the potential of FMN@BSA NPs as a promising strategy and a clinical translational approach for the treatment of lung injury-caused PF.

2. Materials and methods

2.1. Materials

All chemicals were of analytical grade. Formononetin and bovine serum albumin were purchased from Aladdin Reagent Co. Ltd. (Shanghai, China). DID, Coumarin 6, LPS, Z-VAD-FMK, and BODIPY 493/503 were obtained from Beyotime (Shanghai, China). Nigericin was purchased from Macklin Biochemical Co., Ltd (Shanghai, China). Bleomycin was obtained from Nippon Kayaku Co., Ltd (Tokyo, Japan). Cell counting kit-8 (CCK-8), Annexin-V-FITC/PI, Hoechst 33258, and DAPI were the products of KeyGen Biotech (Nanjing, China). RIPA lysis buffer and other reagents related to western blot assays were obtained from Solarbio Science & Technology Co., Ltd (Beijing, China). *Anti*-caspase-1 antibody (24232), anti-GSDMD antibody (39754), anti-NLRP3 antibody (15101), anti-ASC/TMS1 antibody (67824) were purchased from Cell Signaling Technology, Inc (MA, USA). *Anti*-α-SMA antibody (A17910), anti-COL1A1 antibody (A1352), anti-FITC-IgG (H+L) antibody (AS011) were obtained from Abclonal Technology Co. Ltd. (Wuhan, China). *Anti*-SPARC antibody (ab55847) was obtained from Abcam (Cambridge, UK). Pirfenidone was obtained from Med Chem Express (NJ, USA). Recombinant mouse transforming growth factor-β1 (TGF-β1) was purchased from Absin (Beijing, China). Fetal bovine serum (FBS), Dulbecco's modified eagle medium (DMEM), trypsin-EDTA (0.25%), and penicillin-streptomycin stock solutions were obtained from Invitrogen Co., Carlsbad, CA, USA. All the other chemical reagents and solvents were obtained from Sinopharm Chemical Reagent Co., Ltd (Shanghai, China).

2.2. Animals and cell culture

Bone marrow cells were extracted from the femur and tibia of male C57 mice [29]. After centrifugation at 300×*g* for 5 min, erythrocytes were removed, and the remaining cells were cultured in DMEM containing 10% FBS and 20 ng/mL macrophage colony-stimulating factor (M-CSF, MCE, USA). The culture medium was exchanged every three days, and adherent BMDMs were obtained after 6–7 days. Mouse embryo fibroblast cell lines (NIH3T3) were purchased from the Cell Bank of Chinese Academy of Sciences (Shanghai, China) and cultured in DMEM containing 10% FBS at 37 °C in a humidified atmosphere with 5% CO_2. ATCC authenticated cell lines.

Male C57 mice 6- to 8-week-old were obtained from SLAC Animal Ltd. (Shanghai, China) and raised under standard housing conditions of the Department of Experimental Animals, Fudan University (Shanghai, China). All the animal experiments were conducted following guidelines evaluated and approved by the Institutional Animal Care and Use Committee (IACUC), School of Pharmacy, Fudan University (Shanghai, China).

2.3. Cytotoxicity assay

Cell viability was investigated by CCK-8 assay. 5×10^3 cells per well were seeded overnight in 96-well plates and subsequently incubated with different concentrations of drugs. The CCK-8 reagent was added to the cells and incubated for 1.5 h at 37 °C, then assessed at 490 nm by a microplate reader (Thermos Multiskan MK3, USA).

2.4. LDH release assay

For pyroptosis and inflammasome activation, BMDMs were excited with ultrapure LPS (100 ng/mL) for 3 h and treated with an indicated dosage of FMN or FMN@BSA NPs for 1 h, stimulated with nigericin (10 μM, 2 h). Meanwhile, Z-VAD-FMK (20 μM) was used as the positive control drug. After irritation, cell culture supernatant was collected for LDH assay (Beyotime, China) according to the manufacturer's instructions. The absorbance of each well was measured by a microplate reader.

2.5. Interleukin-1β (IL-1β) secretion

The pro-inflammatory molecule IL-1β in cell culture medium suspensions from different treatment groups was detected by ELISA kits (Absin, China). Collected cells were centrifuged for 5 min at 100×*g*, and 100 μL supernatant was moved to a 96-well plate (target protein-specific monoclonal capture antibody had been coated) and hatched for 2 h at room temperature. After rinsing the plate, 100 μL biotinylated antibody was added to each well and hatched for 1 h at room temperature. Subsequently, 100 μL horseradish peroxidase-labeled streptavidin and TMB substrate were added to each well in turn and hatched for 20 min at room temperature away from light. Finally, 50 μL termination solution was added, and the optical density (OD) value at 450 nm was evaluated immediately after mixing.

2.6. Cell morphology observation

BMDMs were seeded into 6-well plates at the density of 1×10^6 cells per well and afterward hatched with various formulations, respectively. The morphology of cells was further observed by phase-contrast microscope (Olympus, Japan). Meanwhile, BMDMs were cultured in confocal dishes. Combined staining with Hoechst 33342 (labeling cell nuclei) and PI (labeling died cells via entry through ruptured cell membranes) was used to detect BMDMs necrosis during the process of pyroptosis. Bright-

field and fluorescent images were recorded under CLSM (Leica, Germany).

2.7. Flow cytometry

As for pyroptosis quantitative analysis, BMDMs with different treatments described above were gathered, washed with PBS thrice, and stained with the Annexin V-FITC/PI kit according to the manufacturer's instructions. Flow cytometry was used to quantify cell death.

2.8. Western blot analysis

To investigate the intrinsic mechanism of FMN blocking BMDMs pyroptosis, relevant proteins (GSDMD-FL, GSDMD-N, pro-caspase-1, cleaved-caspase-1, NLRP3) were selected for immunoblotting analysis *in vitro*. Cells were collected after different treatments described above, and total protein was extracted with lysis buffer. Equal amounts of proteins from various samples were loaded onto SDS-polyacrylamide gels (20 μg protein per path) to separate the target proteins. Proteins were transferred to polyvinylidene difluoride (PVDF) membranes, blocked, and hatched with primary antibody overnight at 4 °C, followed by incubation in goat-*anti*-rabbit IgG H&L (HRP) secondary antibody for 2 h at room temperature. Finally, the strips were imaged with ECL western blot substrate detection and quantified using ImageJ software. The levels of the correlated pyroptosis proteins in mouse lung tissues were similarly detected by the western blot assay described above.

2.9. ASC oligomerization

BMDMs were planted in confocal dishes (5×10^5 cells/dish) and cultured in a complete medium at 37 °C overnight. BMDMs were excited with ultrapure LPS (100 ng/mL) for 3 h and treated with indicated dosage of FMN or Z-VAD-FMK for 1 h, stimulated with nigericin (10 μM, 2 h). After fixation, permeabilization, and blockage, cells were hatched with anti-ASC/TMS1 antibody overnight at 4 °C, then stained with anti-FITC-IgG (H+L) antibody at room temperature. Nuclei were stained by Hoechst 33342, and the ASC speck formation was observed under CLSM (Leica, Germany). The immunofluorescent images were acquired via ZEN software (Carl Zeiss).

2.10. Preparation and characterization of FMN@BSA NPs

FMN@BSA NPs were constructed by the inverse solvent precipitation method to induce self-assembly of FMN with BSA in different weight ratios [22,30]. Firstly, FMN was dissolved in DMSO, and BSA was dissolved in ddH_2O by vortexing. The FMN solution was mixed dropwise into BSA under vigorous stirring for 3 h at room temperature, followed by adding 2 mL EtOH dropwise to the mixture at a rate of 1 mL/min using an automatic syringe pump and stirring for 3 h. The mixture was then transferred to a 20 kDa dialysis bag for dialysis for 48 h. The free drug and organic solvent were removed, followed by lyophilization and weighing, then re-dispersed with sterile PBS and stored at 4 °C for backup. DID or Coumarin 6 labeled FMN@BSA NPs was obtained by a similar procedure as described above, where an ethanol solution of DID or Coumarin 6 was added during the self-assembly of FMN with BSA.

The concentration of BSA in the FMN@BSA NPs suspension was obtained using the BSA kit. To quantify the loading capacity of FMN, FMN@BSA NPs were dissolved in 2 mL of DMSO/ethanol (9:1, v/v) solution and sonicated for 10 min to extract FMN completely. The concentration of FMN were measured by HPLC (Aglient 1260, USA). The drug encapsulation efficiency (EE) and loading capacity (LC) were calculated as follows:

EE (%) = (amount of drugs in nanoparticles)/(total amount of drugs added)×100%

LC (%) = (amount of drugs in nanoparticles)/(nanoparticles weight)×100%

The morphology of FMN@BSA NPs was subsequently observed by TEM and SEM, respectively. The hydrodynamic diameter, PDI of NPs constructed with different ratios of drugs were measured with a dynamic light scattering detector (DLS) (Zetasizer, Nano-ZS, Malvern, UK). The Z-average diameter was monitored for 48 h to monitor the stability of FMN@BSA NPs in saline. Meanwhile, the interaction between FMN and BSA was performed by computer simulation.

2.11. SPARC content detection

Lung tissue samples from BLM-treated mice were removed on the ninth day after modeling, and healthy mice were used as controls. Lung tissues of each group were fixed in 4% paraformaldehyde, paraffin-embedded sections, and immunohistochemical staining was performed for detecting the expression level of SPARC. The sections were observed and photographed under the inverted microscope (Nikon, Japan). Lung tissues were also homogenized to extract proteins, and SPARC protein levels were measured and quantified using the western blot method described previously.

2.12. In vitro co-localization of FMN@BSA NPs with lysosomes

BMDMs were seeded into confocal dishes at a density of 1×10^6 cells per dish. After 24 h, cells were incubated with Cou6-labeled FMN@BSA NPs for a predetermined time (1, 2, and 4 h). Afterward, the cells were stained with Red and Hoechst according to the manufacturer's protocol (Beyotime, China). Then the dishes were imaged on CLSM (Leica, Germany). The immunofluorescent images were acquired via ZEN software (Carl Zeiss).

2.13. Pharmacokinetics study

To confirm that albumin nanoparticles could prolong blood circulation *in vivo*, six C57 mice were randomly assigned into two groups and *i.v.* injected with free DID and DID-FMN@BSA NPs (1 mg/kg of DID), respectively. Blood samples (50 μL) were collected from the orbital sinus into heparin-pretreated polyethylene tubes at pre-designed time points (0.25, 0.5, 1, 2, 4, 8, 12, and 24 h) post-injection. As for the analysis of DID concentration in plasma, the plasma samples were diluted with PBS and subjected to a microplate reader (Thermo Multiskan MK3, USA) (Ex = 644 nm, Em = 665 nm).

2.14. Biodistribution study

On day 9 of lung injury modeling, 100 μL of fluorescently labeled DiD/FMN@BSA NPs (DiD 1 mg/kg) were *i.v.* injected into the C57 mice. The SPARC-block group was also established as a control, and a 50 μg anti-SPARC antibody was injected intraperitoneally 1 h in advance. The biodistribution behavior of nanoparticles *in vivo* was monitored non-invasively at 1, 2, 4, 8, 12, and 24 h by IVIS Spectrum Imaging System (PerkinElmer, USA). The fluorescence distribution of each tissue was photographed *in vitro* and analyzed semi-quantitatively by Living Image software in main organs of the above two groups of mice 24 h after injection.

2.15. Safety study

To assess the *in vivo* safety of the formulation, FMN@BSA NPs (FMN 10 mg/kg) were *i.v.* injected into healthy C57 mice for seven consecutive days, and saline was injected as a control. Representative organ tissues such as heart, liver, spleen, lung, and kidney were collected after the last injection. The tissues were immobilized with 4% paraformaldehyde, paraffin-embedded sections, and stained with H&E, and the slices were observed and photographed under an inverted microscope (Nikon, Japan).

2.16. Scratch assay

NIH3T3 was seeded in 6-well plates, incubated for 24 h, and then attached. The suspended cells were removed by scoring the middle of the well plate with a 200 μL pipette tip, followed by washing the cells three times with PBS. Images were obtained by a phase-contrast microscope (Olympus, Japan). The cells were then treated with the indicated media (DMEM, CM-M^{LPS}, CM-$M^{LPS+Nigericin}$, CM-$M^{LPS+Nigericin+FMN@BSA,}$ TGF-β) for 48 h, and the migration ability was evaluated by phase-contrast microscopy. The conditioned medium (CM) was prepared as follows. BMDMs induced to differentiate with M-CSF were treated with different formulations and incubated with a fresh medium for another 12 h. The supernatant of this culture medium was used as CM. 10 ng/mL of TGF-β was used as a positive control.

2.17. TMT-based proteomics analysis

BMDMs cells treated with PBS, LPS+Nig, and LPS+Nig+FMN@BSA were collected. Three samples were set up for each group. Protein extraction and quantification were performed according to the previous protocol. Protein samples of each group were subjected to SDS-PAGE electrophoresis to check the consistency of each group. Protein samples were 50 μg per group, reduced, alkylated, and digested with trypsin overnight at 37 °C. Each sample solution was then labeled according to the instructions for the TMT labeling reagent. After mixing and labeling, the samples were reversed-phase separated by liquid chromatography (Agilent 1100 HPLC) and vacuum freeze-dried for subsequent use. Samples were stowed at a flow rate of 300 nL/min into a pre-column AcclaimL/min, onto a pre-column Acclaim PepMap100 and then separated by an analytical column Acclaim PepMap RSLC. MS scans were set to full scan charge to mass ratio m/z range of 350–1800 for the 20 highest peaks; all MS/MS acquisition was made using data-dependent high energy collisional cleavage in positive ion mode with collision energy set to 30. The mass spectrometry data were detected using Proteome Discover 2.4 (Thermofisher) database for analysis.

2.18. Metabolomics analysis

For sample preparation for LC-MS metabolomics analysis, BMDM cells were washed with PBS and then frozen in liquid nitrogen and lysed in 80% methanol. 20 μL of L-2-chlorophenyl alanine dissolved in methanol was used as the internal standard. The cells were sonicated in an ice-water bath for 20 min, centrifuged at 13,000 rpm for 10 min, and 800 μL of supernatant was evaporated into LC-MS vials. Subsequently, it was resolubilized, centrifuged, filtered, and analyzed on a liquid mass spectrometer consisting of a Dionex U3000 UHPLC tandem QE plus a high-resolution mass spectrometer. The derivatives were separated using an Acquity UPLC Hss T3 column. The flow rate was 0.35 mL/min at 45 °C, and the injection volume was 5 μL. The mobile phases were A-water (containing 0.1% formic acid) and B-acetonitrile (containing 0.1% formic acid). The mass spectrometry ion source was ESI, and the sample spectra were acquired in both positive and negative ion scan mode. Finally, mass spectral information was resolved in the metabolomics data processing software Progenesis QI v2.3.

2.19. Lipid content measurement

For semi-quantitative analysis of lipid content, BMDMs from different treatments were collected, washed three times with PBS, stained with 2 μM BODIPY 493/503 at 37 °C for 15 min, followed by preparation of single-cell suspensions, washed with PBS, and examined by flow cytometry. Triglyceride levels in BMDMs were measured using the TG assay kit (Biosharp, China). Briefly, 5×10^6 cells were collected after the indicated treatments and fragmented with ultrasound, and the supernatants were collected after centrifugation for analysis by the glycerol lipid oxidase (GPOPAP) method. Samples were reacted with the mixture in the kit and incubated for 30 min at room temperature, then assessed at 510 nm by a microplate reader.

2.20. Histological analysis

The lung tissues of each group of mice were gathered and immobilized with 4% paraformaldehyde for more than 48 h, paraffin-embedded and sectioned for H&E and Masson staining, and the degree of lung tissue inflammation and collagen deposition was observed with Olympus Slide View VS200 (Tokyo, Japan). Inflammatory lesions of lung tissue were evaluated according to the Szapiel scoring system [31], and the level of fibrosis was quantified concerning the numerical scale described by Ashcroft [32]. In addition, immunofluorescence staining was conducted on paraffin-embedded sections, which were dewaxed, permeabilized, and blocked. Subsequently, they were stained with DAPI, F4/80 (Alexa flour 488), and GSDMD (Alexa flour 647), observed with Nikon Inverted Fluorescence Microscope (Tokyo, Japan), and photographed.

2.21. Lung injury and fibrosis model establishment and therapeutic efficacy evaluation

Six-to eight-week-old male C57 mice were used to construct a BLM-induced pulmonary injury model. Briefly, mice were anesthetized and underwent a tracheotomy, and a single dose of 2.5 U/kg of 50 μL of PBS solution containing BLM was administered intratracheally using a microfluidic nebulization device. 50 μL of PBS solution was administered similarly to establish the sham-operated group. Five days after modeling, mice were started to receive *i.v.* injections of PBS, FMN@BSA NPs (FMN 10 mg/kg) or PFD (50 mg/kg) once every two days. On day 14, CT scans of the mice's lungs were performed using Siemens Micro-CT (Berlin, Germany) to observe model establishment's success and assess the treatment effect initially [33]. On day 21, 5 mice from each group were sacrificed, and samples were subjected for further analysis. The remaining eight were observed for survival until the end of 40 days after modeling.

Bodyweight changes of each group of mice were recorded during the modeling and treatment period and weighed every three days. Within 24 h after receiving the last treatment, the lung function of each group of mice was thoroughly evaluated using a BUXCO small animal lung function instrument (DSI, USA). Mice were intubated under anesthesia to measure respiratory data. The trachea and lungs of mice were subsequently separated, and lavage apparatus was inserted into the left bronchus. The appropriate amount of PBS solution was injected and lavaged 2–3 times, 0.3 mL each time, and the BALF solution was collected, centrifuged, and the supernatant was aspirated and stored in a refrigerator at −80 °C for backup. The cell precipitate was resuspended with 100 μL PBS, and the inflammatory cells were counted using a small animal cell sorting counter. The serum after centrifugation of blood taken from mouse orbits and the supernatant solution after centrifugation of BALF were collected and subjected to ELISA to detect changes in relevant inflammatory factors, respectively. Fresh lung tissues were removed and frozen at −80 °C in the refrigerator for subsequent western blot analysis. The assay for intrapulmonary hydroxyproline was performed according to the instructions of the HYP kit obtained from Jiancheng Bioengineering Institute (Nanjing, China).

2.22. Statistical analysis

All data were expressed as mean ± standard deviation (SD). Two groups were compared using unpaired student's t-test, and multi-group analysis was performed using one-way ANOVA and Bonferroni tests. *$P < 0.05$, **$P < 0.01$, and ***$P < 0.001$ indicated statistical difference and n. s. signified no critical change.

3. Results and discussions

3.1. FMN inhibits macrophage pyroptosis induced by NLRP3 inflammasomes

To examine the effect of FMN on macrophages *in vitro*, we first determined its cytotoxicity to bone marrow-derived macrophages (BMDMs). Since no obvious toxicity was observed up to 50 μM (Fig. 1A), we selected 12.5, 25, and 50 μM as low, medium, and high concentrations of FMN for the following investigations. Then we treated BMDMs with lipopolysaccharide (LPS) and nigericin to establish the *in vitro* pyroptotic macrophage model. As shown in Fig. 1B and C, macrophages showed severe lactate dehydrogenase (LDH) and IL-1β release after exposure to LPS and nigericin, which could be significantly inhibited by FMN treatments, could inhibit the process in a dose-dependent manner. Under phase-contrast microscopy, BMDMs underwent cell swelling and membrane blebbing after LPS+Nigericin stimulation, presenting typical cell morphology of pyroptosis (Fig. 1D) [34]. The number of spherical macrovesicles and tentacles on the membrane was significantly reduced after FMN intervention, while the degree of cell swelling gradually decreased with increasing FMN concentration. Finally, the Annexin V/PI assay was used to quantify the pyroptotic macrophages presented as PI-positive cells. The flow cytometry analysis suggested that FMN could inhibit macrophage pyroptosis induced by LPS and nigericin in a dose-dependent manner (Fig. 1E). The above results demonstrated that FMN could significantly mitigate the pyroptosis process in macrophages.

To further reveal the underlying mechanism, we investigated the impact of FMN on protein expression levels of NLRP3 and pyroptosis-related markers. After pathological stimulation on alveolar macrophages, the intracellular NLRP3 proteins will be activated and assembled with adaptor protein and pro-caspase-1 to form inflammasomes. Then, inflammasomes release the cleaved-caspase-1, which subsequently triggers the cleavage of GSDMD to generate the GSDMD-nitrogen terminal. The western blot assay showed that FMN efficiently reversed the upregulation of NLRP3, GSDMD-N, and cleaved-caspase-1 caused by LPS+Nigericin (Fig. 1F and G). Following the treatment of FMN with a high concentration, the inhibition effect on protein expression of NLRP3 and pyroptosis markers in macrophages was comparable to that in those cells treated with the pan-caspase inhibitor, Z-VAD-FMK. These results demonstrated that FMN successfully decreased NLRP3 expression and thus blocked caspase-1 activation, thereby reducing the cleavage of GSDMD. To further verify the FMN-mediated blockage of the NLRP3 pathway, the adaptor protein of the NLRP3 inflammasome, apoptosis-associated speck-like protein containing a CARD (ASC), was detected through immunofluorescent staining [35]. After the treatment with LPS+Nigericin, many ASC specks formed in the cytoplasm of macrophages (Fig. 1H), indicating NLRP3 inflammasome activation. FMN could efficiently reduce the number of ASC specks. Especially, FMN at a concentration of 50 μM almost eliminated the ASC oligomerization like Z-VAD-FMK. Taken together, these results confirmed that free FMN could serve as an inhibitor to relieve macrophage pyroptosis through intervening NLRP3 inflammasome activation.

3.2. Preparation and characterization of FMN@BSA NPs

Prior to the preparation of the actively targeting nanoformulation, we established the bleomycin (BLM)-induced lung injury and fibrosis model and investigated the SPARC expression in the impaired lung tissues. Based on the immunohistochemical staining and WB analysis, lung tissue collected from the BLM-treated mice exhibited significantly elevated SPARC protein compared to the healthy lungs (Fig. 2A and B). Overexpression of SPARC protein inside the impaired lesions encouraged us to design the albumin-based nanoparticles to actively deliver FMN by maximizing the high affinity between SPARC and albumin. We used bovine serum albumin (BSA) to prepare the FMN-containing nanoparticles, FMN@BSA NPs, through the nanoprecipitation method. Based on the size and polydispersity index (PDI), we screened a range of nanoparticles with different mass ratios of BSA and FMN to find the optimal formulations (Fig. S1). We found that the favorable ratios were 20:1 and 37.5:1 within our condition, which showed the most appropriate size. Based on the consideration of drug loading efficiency, 20:1 was selected as the optimal ratio between albumin and FMN to prepare the final nanoparticles. As shown in Fig. 2C, the albumin nanoparticles with the ratio of 20:1 (BSA/FMN) showed a narrow size distribution with an average size of 148.8 ± 19.3 nm and PDI of 0.122. The appearance of FMN@BSA NPs became white emulsions with a pronounced Tyndall effect after laser irradiation, which was consistent with the characteristics of nanoscale particles. Under scanning electron microscopy (SEM) and transmission electron microscopy (TEM), FMN@BSA NPs displayed a uniform spherical structure with particle sizes ranging from 120 to 150 nm (Fig. 2D). The UV–vis spectra of FMN@BSA NPs showed absorption peaks around 300–330 nm and 270 nm corresponding to FMN and BSA, respectively (Fig. S2), and the drug loading capacity and loading efficiency of FMN in FMN@BSA NPs was 4.75% and 52.5%, which quantified via high-performance liquid chromatography (HPLC). We used molecular dynamics simulations to understand the structural mechanisms of the albumin-loaded FMN to examine the stability of the relevant conformations. As shown in Fig. 2E, FMN was well embedded in the cavity at the interface of albumin. The residues LYS-136 and ILE-181 form hydrogen bonds with the small molecules and could build a stable crystal structure. As shown in Fig. 2F, FMN@BSA NPs exhibited slight changes in size and PDI with incubation in saline for 48 h, indicating good stability. Moreover, FMN@BSA NPs were maintained stably in deionized water, phosphate-buffered saline (PBS), culture media, and 10% fetal bovine serum (FBS) (Fig. S3). No obvious toxicity was observed in both BMDMs and NIH3T3 cells after the nanoparticle treatment at the FMN concentration of 50 μM, demonstrating the favorable safety profiles of FMN@BSA NPs (Fig. 2G). We prepared Cou6-labeled FMN@BSA NPs to observe drug release behavior in BMDMs. As shown in Fig. S4, Cou6/FMN@BSA appeared co-localized with lysosomes after 1 h, while Cou6 entered from lysosomes to cytoplasm showing intense green light after 4 h. It proves that the albumin nanoparticles can be degraded by the acidic environment and hydrolytic enzymes after entering the lysosomes to achieve the release of the loaded drug.

Subsequently, 1,1′-dioctadecyl-3,3,3′,3′-tetraMethylindodicarbocyanine perchlorate (DiD)-labeled nanoparticles (DiD/FMN@BSA NPs) were employed to investigate the *in vivo* behavioral properties of the nanoparticles. As shown in Fig. S5, DID/FMN@BSA demonstrated a longer blood circulation time than free DID, while DID/FMN@BSA had significantly higher blood retention (11.0% ID/g) at 24 h after injection than free DID (3.20% ID/g), which contributed to the effective accumulation of FMN@BSA NPs at the lung lesion site. After intravenous injection (*i.v.*) of free DiD or DiD/FMN@BSA NPs, the biodistribution was evaluated by the *in vivo* imaging system (IVIS) spectrum. The results showed that fluorescence signals in DiD/FMN@BSA NPs treated lung tissues were gradually enhanced in a time-dependent manner, reached a maximum at 8 h, and largely retained even at 24 h (Fig. 2H). In contrast, free DiD accumulated mainly in the liver and was quickly cleared. The main organs (heart, liver, spleen, lung, and kidney) were then subjected to imaging at 24 h after administration. The fluorescence intensity of DiD/FMN@BSA NPs in the lungs further verified the excellent lung tissue enrichment of FMN@BSA NPs. Besides, we explored the role of SPARC protein-BSA interaction to further reveal the underlying mechanism of preferential accumulation. The pretreatment with the antibody against SPARC protein, which can block the binding of BSA to SPARC, dramatically impaired the accumulation of DiD/FMN@BSA NPs in the lungs. Similarly, reduced lung accumulation of DiD fluorescence was also observed in *ex vivo* lung tissues after the anti-SPARC antibody

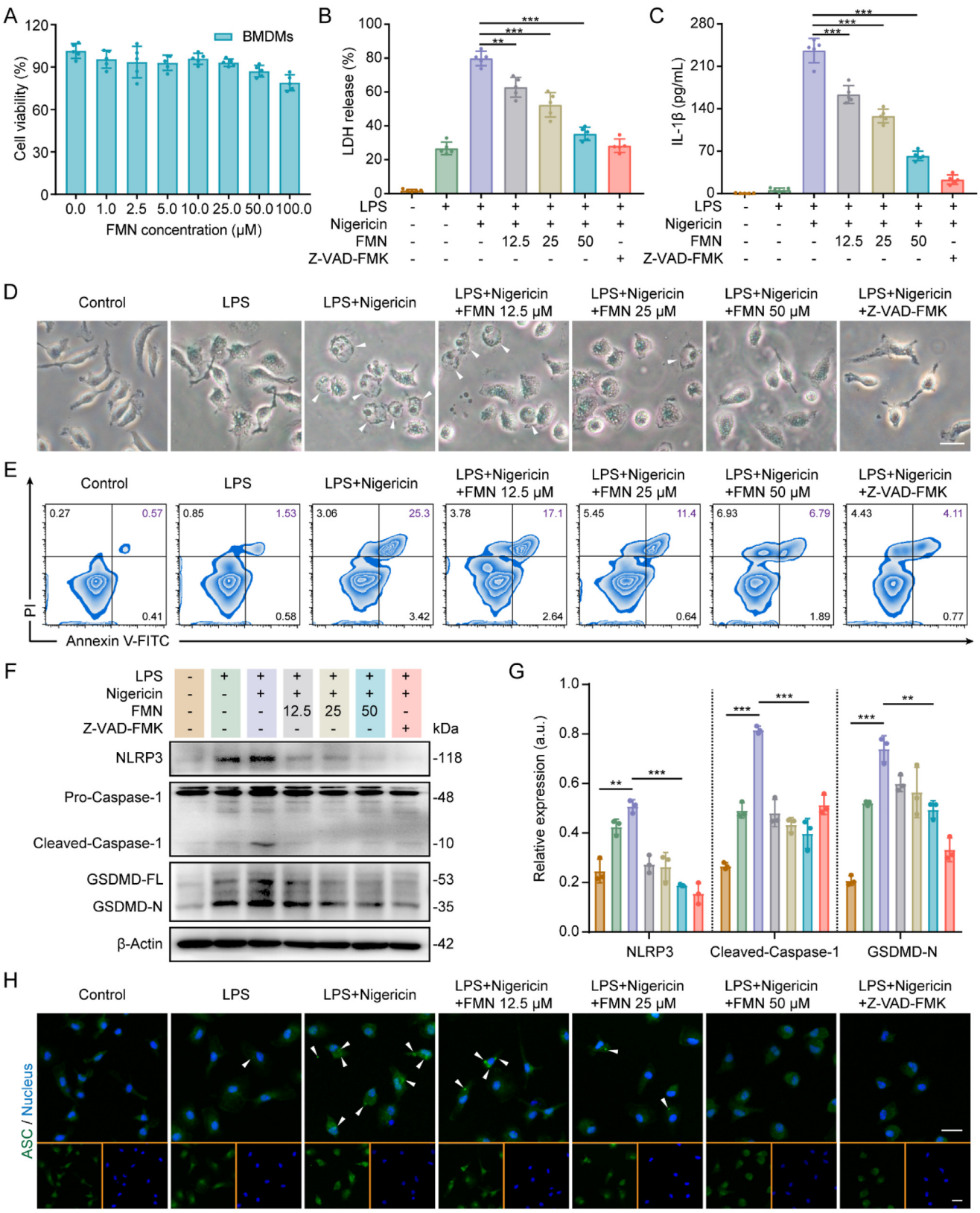

Fig. 1. FMN inhibits macrophage pyroptosis induced by NLRP3 inflammasomes. A) Relative viabilities of BMDMs treated with FMN at various concentration. Data were represented as mean ± SD (n = 5). B) LDH or C) IL-1β release from BMDMs cells after the indicated treatments. Data were represented as mean ± SD (n = 5). D) Cell morphology of BMDMs after the indicated treatments. White arrows indicate the pyroptotic cells. Scale bar, 8 μm. E) Flow cytometry analysis of the pyroptotic BMDMs after the indicated treatments with Annexin-V/PI double staining. F, G) Expression of NLRP3 and pyroptosis-related proteins (GSDMD-FL, GSDMD-N, pro-caspase-1, cleaved-caspase-1) in BMDMs after the indicated treatments. Data were represented as mean ± SD (n = 3). H) IF staining ASC (green) in BMDMs after the indicated treatments. Hoechst (blue) indicates nuclei. Scale bar, 10 μm. (For interpretation of the references to colour in this figure legend, the reader is referred to the Web version of this article.)

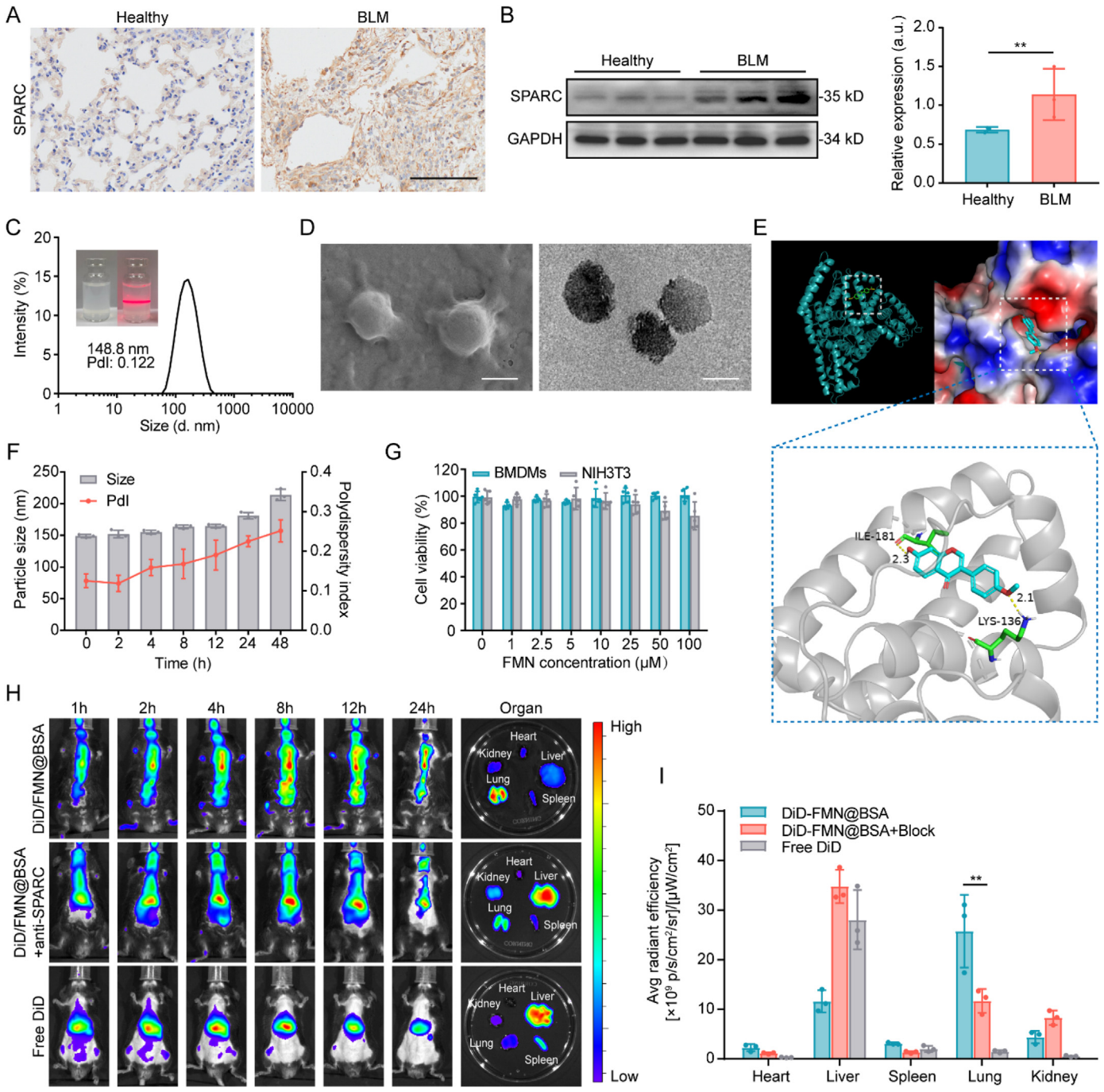

Fig. 2. Preparation and characterization of FMN@BSA NPs. A) Immunohistochemical staining of lung tissues collected from healthy and BLM-treated mice. Scale bar, 100 μm. B) Western blotting analysis of SPARC expression in lung tissues of healthy and BLM-treated mice. Data were represented as mean ± SD (n = 3). C) Size and distribution of FMN@BSA NPs in saline. Inset: the photos of FMN@BSA NPs in saline and its Tyndall effect. D) Morphology of FMN@BSA NPs detected by SEM and TEM. Scale bar, 100 nm. E) Molecular dynamics simulation of FMN and BSA. F) Size and PDI changes of FMN@BSA NPs in saline within 48 h. Data were represented as mean ± SD (n = 3). G) Relative viabilities of BMDMs treated with FMN@BSA NPs at various FMN concentrations. Data were represented as mean ± SD (n = 5). H) Distribution of DiD-labeled FMN@BSA NPs at 1, 2, 4, 8, 12 and 24 h after intravenous injection in murine lung injury model with or without anti-SPARC antibody pretreatment. *Ex vivo* tissues were collected at 24 h post-injection. I) Quantitative analysis of fluorescence signals in *ex vivo* organs at 24 h post-injection. Data were represented as mean ± SD (n = 3).

pretreatment (Fig. 2I). These results demonstrated that the efficient accumulation of FMN@BSA NPs in lung tissues of BLM-treated mice was credited to the high affinity between BSA and SPARC. Notably, there still was lung accumulation of DiD/FMN@BSA NPs after SPARC-blocking, which might be due to higher nutritional demands of cells in the inflammatory environment. To further assess the safety of FMN@BSA NPs, healthy mice were *i.v.* injected with nanoparticles (10 mg/mL FMN) for seven consecutive days, the histological appearance of the major organs was evaluated through hematoxylin and eosin (H&E) staining after the last treatment. No significant morphological changes were noted in any of the organs (Fig. S6), indicating that the nanoparticles did not induce gross abnormal effects in these major organs. In addition, the hematological analysis also demonstrated the good *in vivo* safety of the formulations (Fig. S7).

3.3. FMN@BSA NPs block macrophage pyroptosis to reduce the activation of fibroblasts in vitro

Prior to evaluating the treatment efficacy of FMN@BSA NPs against lung injury and fibrosis, we tested the inhibitory effect of the nanoparticles on macrophage pyroptosis *in vitro*. As shown in Fig. 3A and B, the treatment with FMN@BSA NPs (50 μM FMN) significantly reduced the release of LDH and IL-1β from the pyroptotic BMDMs, and the effect was similar to Z-VAD-FMK. Compared to the free drug FMN, the improved anti-pyroptosis potency of FMN@BSA NPs might be ascribed to the nanoparticle-mediated enhanced internalization into macrophages. Besides, the PI staining showed that FMN@BSA NPs could efficiently decrease the number of pyroptotic BMDMs (Fig. 3C). Specifically, the impaired cytomembrane integrity caused by LPS+Nigericin presented as PI-positive cells along with cell ballooning. In contrast, these phenomena were significantly reduced after the treatment of FMN@BSA NPs. The expression levels of representative proteins related to pyroptosis were shown in Fig. 3D, where FMN@BSA NPs intervention reversed the elevated expression of GSDMD-N and cleaved-caspase-1 in BMDMs caused by the LPS and nigericin treatment. Collectively, these results confirmed that FMN-loaded albumin formulations possessed a remarkable ability to inhibit macrophage pyroptosis, even better than free FMN.

During the initiation and progression of lung injury, an intense inflammatory environment can activate myofibroblasts to secrete matrix proteins [10]. To clarify the activation mechanism of myofibroblasts and verify the crucial role of macrophage pyroptosis in extracellular protein deposition, we collected the conditioned medium (CM) of macrophages with various treatments to incubate NIH3T3 cells and observed the phenotype changes in NIH3T3 cells. As shown in Fig. 3E, conditioned medium from pyroptotic macrophages (CM-Mp) significantly accelerated the migration and wound healing of NIH3T3 cells. These results were similar to the impacts of transforming growth factor-β (TGF-β), a known cytokine that drives fibrosis in multiple diseases [36], indicating that the secreted cytokines from pyroptotic macrophages could activate fibroblasts. In contrast, no obvious cell migration was evaluated in NIH3T3 cells after incubation with the CM collected from the FMN@BSA NPs-treated pyroptotic macrophages (CM-$Mp^{FMN@BSA}$). Moreover, α-smooth muscle actin (α-SMA) was chosen as the activation marker of myofibroblasts to see whether the FMN@BSA NPs-treated pyroptotic macrophages would be conductive to relieving fibrosis progression [37]. It was found that the increased protein level of α-SMA in NIH3T3 is similar to that in those cells incubated with TGF-β. Following the treatment with CM-$Mp^{FMN@BSA}$, the α-SMA expression in NIH3T3 cells was significantly reduced, indicating the deactivating of fibroblasts (Fig. 3F). These results suggested that the intense inflammatory environment caused by macrophage pyroptosis could activate myofibroblasts and that

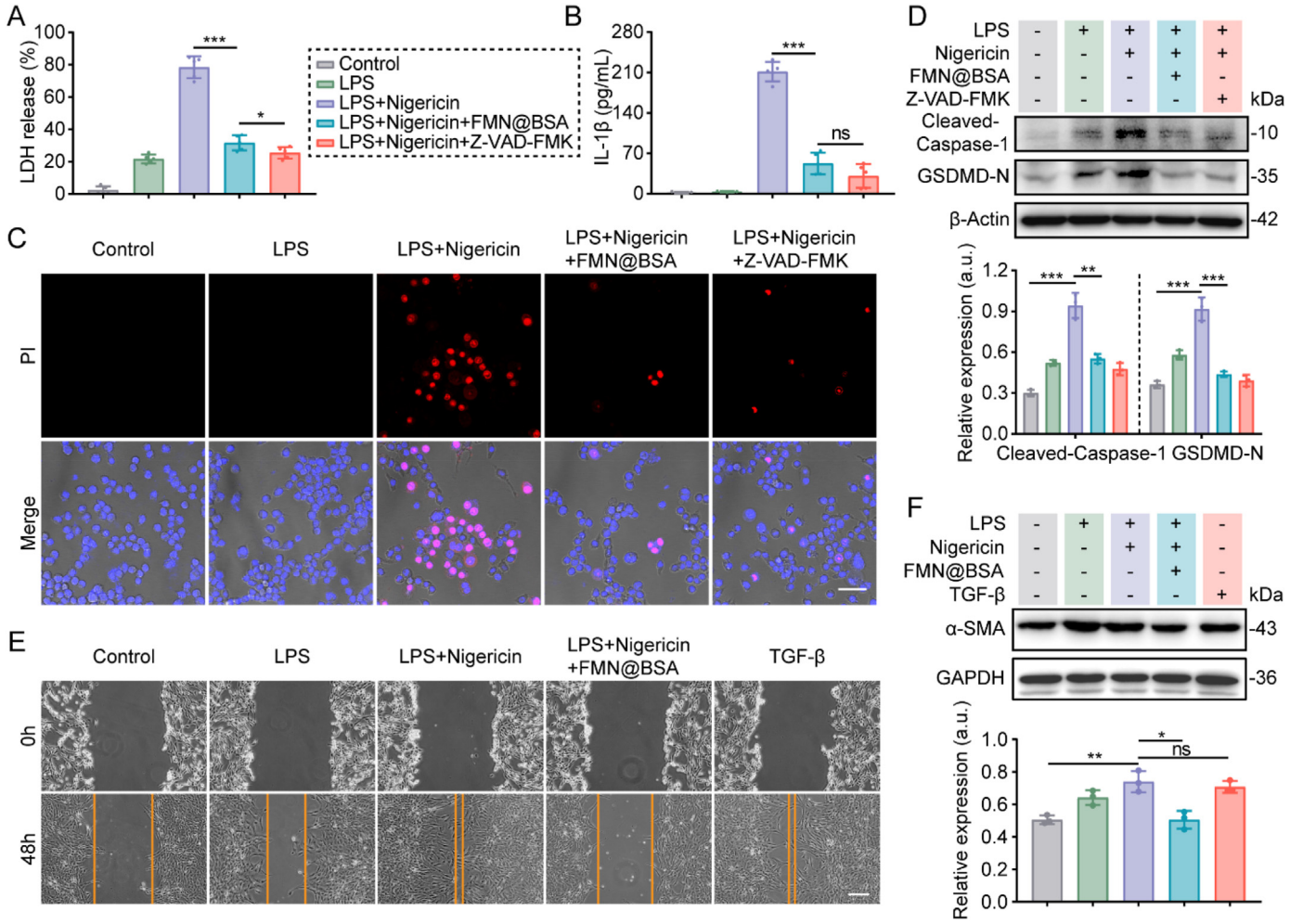

Fig. 3. FMN@BSA NPs block macrophage pyroptosis to reduce the activation of fibroblasts *in vitro*. A) LDH release from BMDMs after the indicated treatments. Data were represented as mean ± SD (n = 5). B) IL-1β release from BMDMs after the indicated treatments. Data were represented as mean ± SD (n = 5). C) PI staining and bright field observation of macrophages after the indicated treatments. Scale bar, 20 μm. D) Western blotting analysis of expression and quantification of pyroptosis-related proteins (GSDMD-N, cleaved-caspase-1) in BMDMs after the indicated treatments. Data were represented as mean ± SD (n = 3). E) Cell scratch assay of NIH3T3. Scale bar, 100 μm. F) Expression and quantitative analysis of fibrosis-associated proteins. Data were represented as mean ± SD (n = 3).

FMN@BSA NPs could block the pyroptosis process in macrophages to mitigate lung injury and fibrosis progression.

3.4. FMN@BSA NPs block macrophage pyroptosis and mitigate inflammation and stroma deposition in vivo

To access the *in vivo* inhibitory effects of FMN@BSA NPs on repolarizing macrophage pyroptosis, mice suffering from BLM were intravenously injected with PBS, nanoparticles, or PFD. Mice following the same procedures as BLM-treated mice were handled with PBS, not BLM, to establish the sham-operated group [38]. From the fifth day, PBS, FMN@BSA NPs, or PFD was administered every other day for 5 times, and the samples were collected for the relevant analysis on the day after the last administration, day 14, which is regarded as the PF formation phase [39]. As shown in Fig. 4A, serum and bronchoalveolar lavage fluid (BALF) collected from BLM-treated mice exhibited significantly higher IL-1β levels than the sham-operated group. However, treatments with FMN@BSA NPs or PFD could significantly attenuate the level of IL-1β in serum and BALF, suggesting the anti-inflammatory effects of the nanoparticle and positive control drug. The immunoblotting experiments revealed a significant increase of pyroptosis-related proteins, cleaved-caspase-1 and GSDMD-N, in lung tissues of BLM-treated mice (Fig. 4B). The upregulation of these proteins could be dramatically reversed by FMN@BSA NPs but not PFD. A similar profile was also reflected in the detection of NLRP3 expression (Fig. S8). Moreover, BALF of BLM-treated mice showed a high concentration of LDH, which could be downregulated by FMN@BSA NPs treatment (Fig. 4C). The above results suggest that FMN@BSA NPs have an excellent effect of blocking NLRP3 activation and thus inhibiting pyroptosis *in vivo*. To further confirm the inhibition effect of FMN@BSA NPs on pyroptosis in macrophages, immunofluorescent staining was performed to determine in which cell populations pyroptosis occurs and would be blocked by the nanoparticles within lung tissue. The right middle lobes in each group were then collected for the paraffin section. A fluorescent F4/80 antibody was used to label alveolar macrophages, and the pyroptotic cells were indicated by GSDMD-N [40]. As shown in Fig. 4D, the red fluorescence of GSDMD-N was obviously elevated in the BLM group and showed a considerable overlap with the green fluorescence of macrophages, indicating that

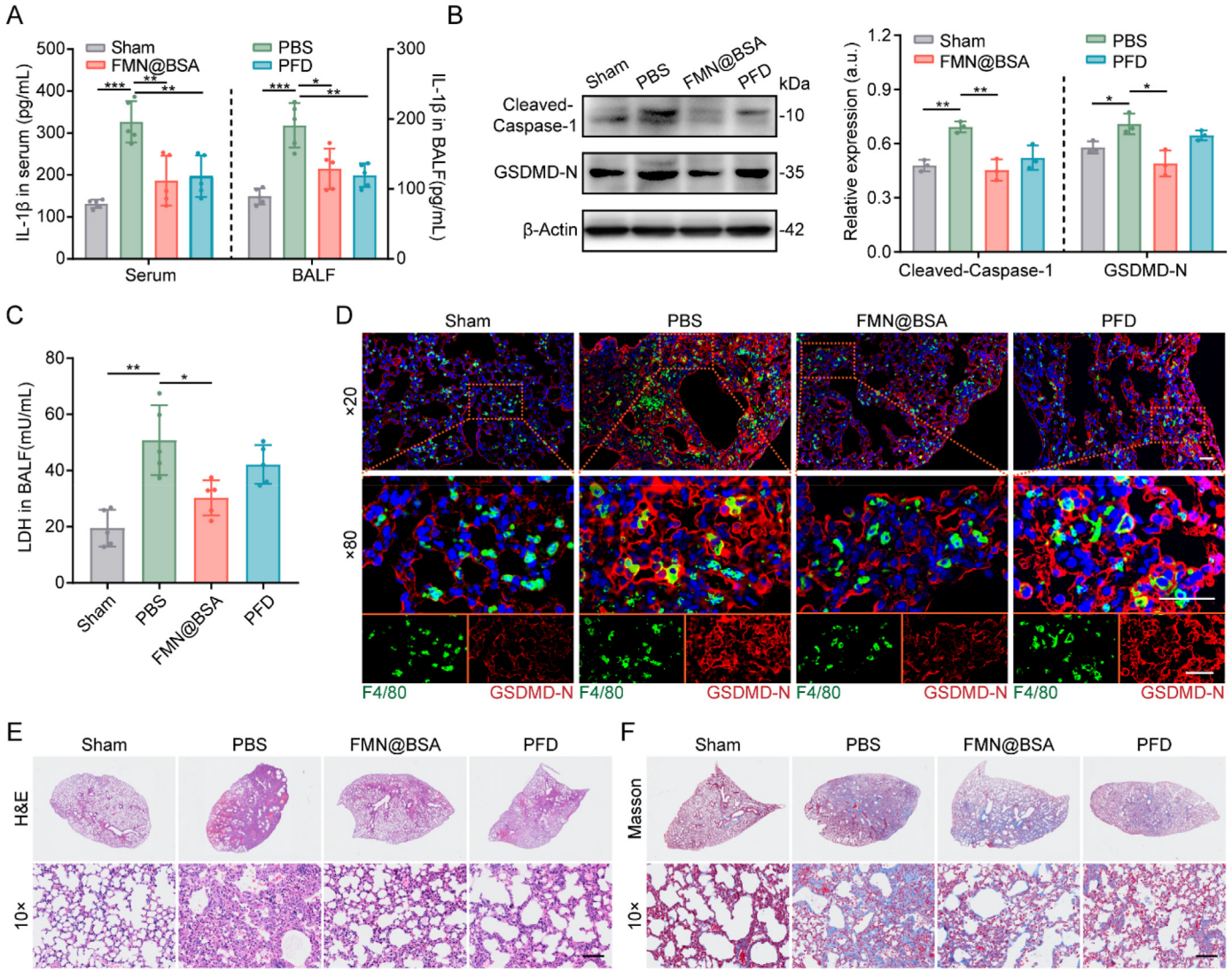

Fig. 4. Inhibitory effect of macrophage pyroptosis of FMN@BSA NPs *in vivo*. A) Content of IL-1β in serum and BALF collected from BLM-treated mice after the indicated treatments. Data were represented as mean ± SD (n = 5). B) Western blotting and quantitative analysis of pyroptosis-associated proteins (cleaved-caspase-1 and GSDMD-N) in lung tissues collected from BLM-treated mice after the indicated treatments. Data were represented as mean ± SD (n = 3). C) Content of LDH release in BALF collected from BLM-treated mice after the indicated treatments. Data were represented as mean ± SD (n = 5). D) Fluorescence images of GSDMD-N (red) and F4/80 (green) distribution in pulmonary tissue after the indicated treatments. The nuclei were stained with DAPI (blue). Scale bar, 50 μm. E) H&E and F) Masson staining of lung sections. Scale bar, 100 μm. (For interpretation of the references to colour in this figure legend, the reader is referred to the Web version of this article.)

pyroptosis in injured and fibrotic lung tissues mainly occurred on alveolar macrophages. Compared to PFD, the GSDMD-N upregulation in macrophages was significantly reduced after the treatment with FMN@BSA NPs. Collectively, while PFD could exert anti-inflammation potency, we suggested that FMN@BSA NPs could mitigate the inflammation reaction and fibrosis through blocking the pyroptosis process in macrophages.

Moreover, at 24 h post-injection of the final formulations, the histological appearance and collagen fiber of the right middle lobes were evaluated to identify the therapeutic effects of the nanoparticle as indicated by the H&E staining and Masson staining, respectively. The results demonstrated that BLM stimulation caused severe alveolar hemorrhage, edema, alveolar septal thickening, and inflammatory cell infiltration, whereas these changes were significantly reduced after FMN@BSA NPs treatment (Fig. 4E, S9). According to the Masson staining, the sections of BLM-treated mice with the treatment of FMN@BSA NPs exhibited a significantly reduced extent of collagen in the lung tissue (Fig. 4F, S10). Besides, the lung tissues of BLM-treated mice administrated with the nanoparticle at the FMN concentration of 10 mg/kg showed improved interstitial structure and normalized alveolar tissue, consistent with the efficacy of the standard treatment of PFD with a commonly used dose of 50 mg/kg. We also set up FMN injection alone as a control group to cure BLM-treated mice. However, due to the highly hydrophobic character of FMN, we prepared an equivalent dose of the suspension for intraperitoneal injection. Pathological results showed that treatment with FMN alone did not significantly alleviate the alveolar inflammation and collagen deposition (Fig. S11). Considering the poor physicochemical characteristics and unfavorable lesion accumulation of free FMN, further evaluating the drug efficacy using an intravenous albumin-loaded FMN formulation is more reasonable. Overall, FMN@BSA NPs exhibited efficient anti-inflammatory and anti-fibrotic abilities in murine lung injury and fibrosis models.

3.5. Multi-omics joint analysis

Based on the abovementioned inhibition effect of FMN@BSA NPs on macrophage pyroptosis, we further explored the relevant mechanism by integrating multi-omics analysis. Other than disorders mainly caused by genetic mutations, the pathogenic changes of pyroptotic macrophages are usually implicated in inflammatory signaling, redox homeostasis, mitochondrial dysfunction, and energy metabolism [41,42]. Therefore, we focus on quantifying the proteins' expression and metabolites and analyzing their associations between different biological layers, thereby revealing the potential acting pathway of the nanoparticle. We first subjected various macrophage samples, including BMDMs control, pyroptotic BMDMs, and pyroptotic BMDMs with the treatment of FMN@BSA NPs, to tandem mass-tagging (TMT)-based proteomics analysis. Specifically, through quantifying the expression of 6066 plausible proteins, principal component analysis (PCA) demonstrated that the total variation was 55.17% (Fig. 5A). Based on the Venn diagram and clustering heat map, there were significant differences in primary protein sources among Control, LPS+Nig, and LPS+Nig+FMN@BSA groups (Figs. S12 and S13). As we were concerned that FMN@BSA NPs could reverse the expression of differential proteins associated with pyroptosis, such as Il1b (Interleukin-1 beta), Cxcl10 (*C*-X-C motif chemokine 10), Hmgb1 (High mobility group protein B1), Il1α (Interleukin-1 alpha), Il4r (Interleukin-4 receptor subunit alpha), Tnf (Tumor necrosis factor) and other inflammatory signaling molecules that exhibited elevated expression after LPS+Nig stimulation (Fig. 5B). Notably, FMN@BSA NPs significantly downregulated the expression of Gsdmd, the direct performer of pyroptosis, Casp1, and Nlrp3, while the level of the Gsdme, another pyroptosis executor, and other caspase proteins showed unnoticeable changes. These results confirmed that FMN@BSA NPs could block the pyroptosis process in macrophages by inhibiting the Nlrp3/Casp1/Gsdmd axis. Gene ontology (GO) analysis revealed that the differential proteins between the pyroptotic BMDMs and the treated ones in biological process (BP), cellular component (CC), and molecular function (MF) mainly affected inflammatory response, extracellular space, lysosome, protease binding-related functions and protein transport (Fig. S14). The Kyoto Encyclopedia of Genes and Genomes (KEGG) analysis results were shown in Figs. S15 and 5C, where pyroptosis is mainly involved in Toll-like receptor signaling pathway, antigen processing and presentation, tuberculosis, neutrophil extracellular trap formation, and other immune-related pathways. Compared to pyroptotic macrophages, the nanoparticles exerted their effects on immune-related pathways. Notably, according to our enrichment data, certain mechanisms that FMN@BSA NPs act on are associated with the major pathogenic pathways of the coronavirus disease (COVID-19). The proteomics proved that FMN@BSA NPs could significantly downregulate multiple inflammatory signaling pathways in macrophages and thus block the pyroptosis process leading to mitigatory inflammation reaction.

We next test the changes in metabolites to further explore the nanoparticle-mediated inhibition effect on macrophage pyroptosis. 3268 plausible metabolites were identified by using liquid chromatography-mass spectrometry (LC-MS) untargeted metabolomics. Among them, the differentially expressed metabolites were screened with the conditions of variable important in projection (VIP) greater than 1 and *P*-value less than 0.05 as indicated by volcano plots (Fig. 5D). In comparison with non-pyroptotic BMDMs, the ones undergoing pyroptosis exhibited 206 differential metabolites. Further, after the nanoparticle treatment, there were 199 differential metabolites in pyroptotic BMDMs. The main differentially expressed metabolites were collected and summarized in the cluster heat map as shown in Fig. 5E. It was demonstrated that the intermediates of the tricarboxylic acid cycle, amino acid metabolism, and lipid metabolism were relatively upregulated during the pyroptosis process. The FMN@BSA NPs significantly inhibited the production of lipid-related metabolites such as 3-hydroxyoctadecanoylcarnitine, itaconic acid, and stearoylcarnitine. Moreover, the nanoparticles also upregulated the concentration of glutathione, an important intracellular antioxidant, and thus reduced lipid oxidation. Meanwhile, FMN@BSA NPs altered the levels of 5′-cytidine monophosphate, cytidine, and 5′-uridine monophosphate, indicating its effect on purine nucleotide metabolism. Collectively, in macrophages undergoing pyroptosis, the nanoparticles could perform regulation effects on the abovementioned metabolic procedures to block the amplification of the inflammation response. The KEGG enrichment analysis between the pyroptotic BMDMs with and without the nanoparticle treatment as shown in Fig. S16. Combining the metabolomics analysis with the above proteomics data, we found 61 pathways showed significant changes at both protein and metabolite levels after FMN@BSA NPs treatment (Fig. 5F), including metabolic pathways, thyroid hormone synthesis, necroptosis, lysosome, and aldosterone synthesis and secretion, etc. Subsequently, key regulatory nodes between the pyroptotic BMDMs and the treated ones were identified by pairwise correlation network analysis of differential proteins and metabolites. For better visualization, the functional classification of each node was annotated with DAVID [43]. According to the multi-omics network, lipid metabolism-related nodes (orange) play an important part in the procedures that the nanoparticle combated the macrophage pyroptosis (Fig. 5G). Since NLRP3 can serve as the sensor of cellular homeostasis [44–46], the disturbance of lipid metabolism might trigger an NLRP3 inflammasome-related inflammatory cascade reaction. Coupled with these omics analyses, we proposed that FMN@BSA NPs could inhibit the activation of NLRP3 inflammasomes by regulating lipid metabolism in macrophages, leading to blockage of the pyroptosis process. To prove this concept, we performed a semi-quantitative analysis of lipid content in BMDMs using the lipophilic fluorescent dye BODIPY 493/503. As shown in Fig. S17, a large number of stained lipid droplets were detected within the pyroptotic cell model, while the fluorescence intensity was drastically reduced after the intervention of FMN@BSA NPs, suggesting a decrease in lipid content. Similar results were obtained by intracellular triglyceride assay (Fig. S18). These results showed that FMN@BSA NPs attenuated lipotoxic injury and NLRP3 inflammasome

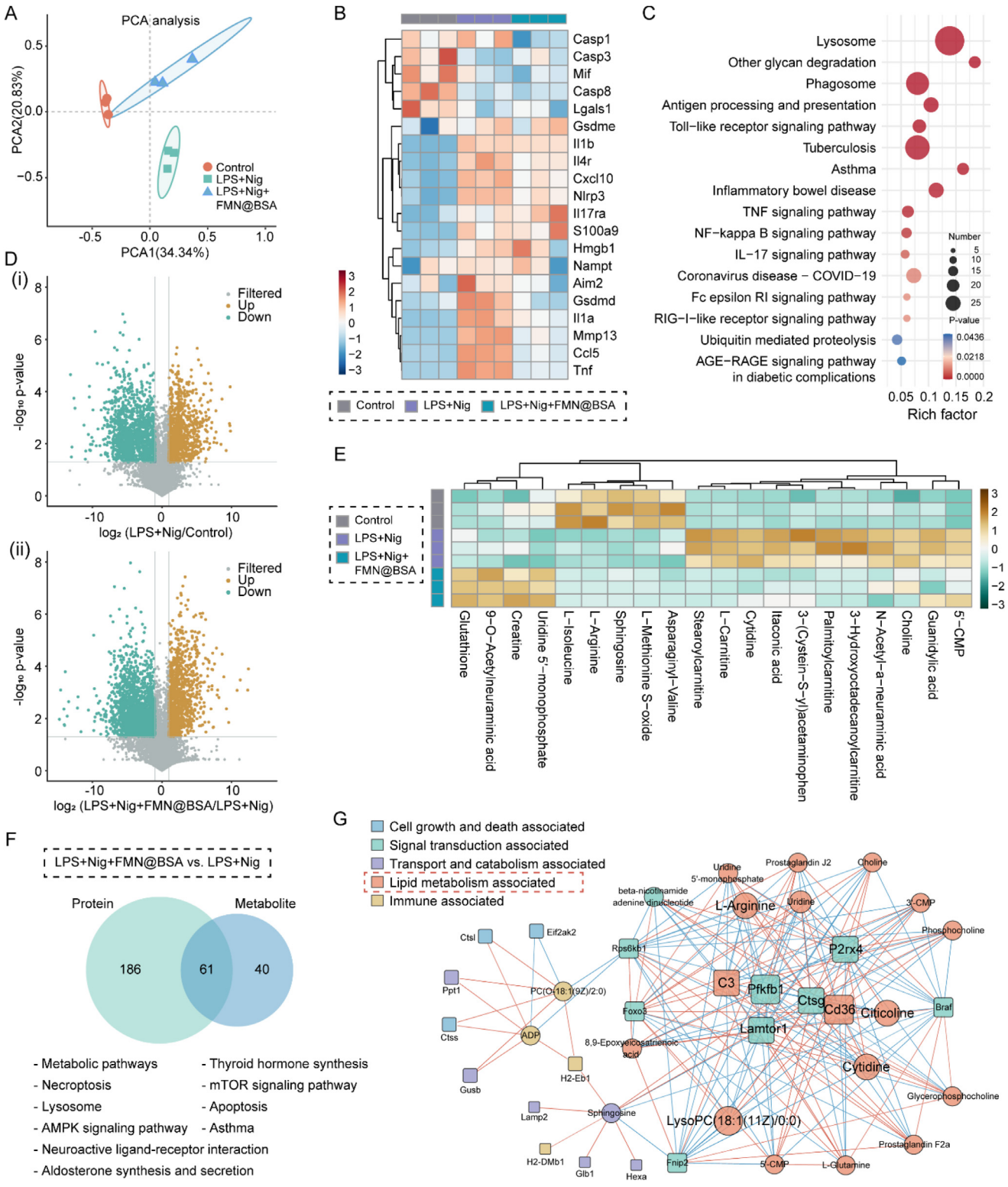

Fig. 5. Combined proteomics/metabolomics analysis. A) Principal component analysis of proteomic data. PCA1 and PCA2 represent the largest source of variation. B) Heat map of differentially expressed proteins associated with pyroptosis in control, LPS+Nig, and LPS+Nig+FMN@BSA groups. C) Bubble plot of the KEGG pathway analysis enriched by differentially expressed proteins between LPS+Nig+FMN@BSA and LPS+Nig groups. The colors of the nodes reflect the p-values of the designated pathways, and the sizes of the nodes indicate the number of differentially expressed proteins enriched in the pathways. D) Volcano plots of differential metabolites in (i) pyroptotic and non-pyroptotic macrophages; (ii) pyroptotic macrophages and treated ones. E) Heat map depicting the differential metabolites clustered between control, LPS+Nig, and LPS+Nig+FMN@BSA groups. F) Venn diagrams illustrating the number of metabolite (blue) and protein (green) pathways significantly changed in pyroptotic BMDMs after FMN@BSA NPs treatment, followed by a list of pathways that were regulated at both the protein and metabolite levels. G) Network analyses illustrating the key functional protein (squares) and metabolite (circles) nodes in pyroptotic BMDMs after FMN@BSA NPs treatment. Nodes were color-coded according to functional classification. (For interpretation of the references to colour in this figure legend, the reader is referred to the Web version of this article.)

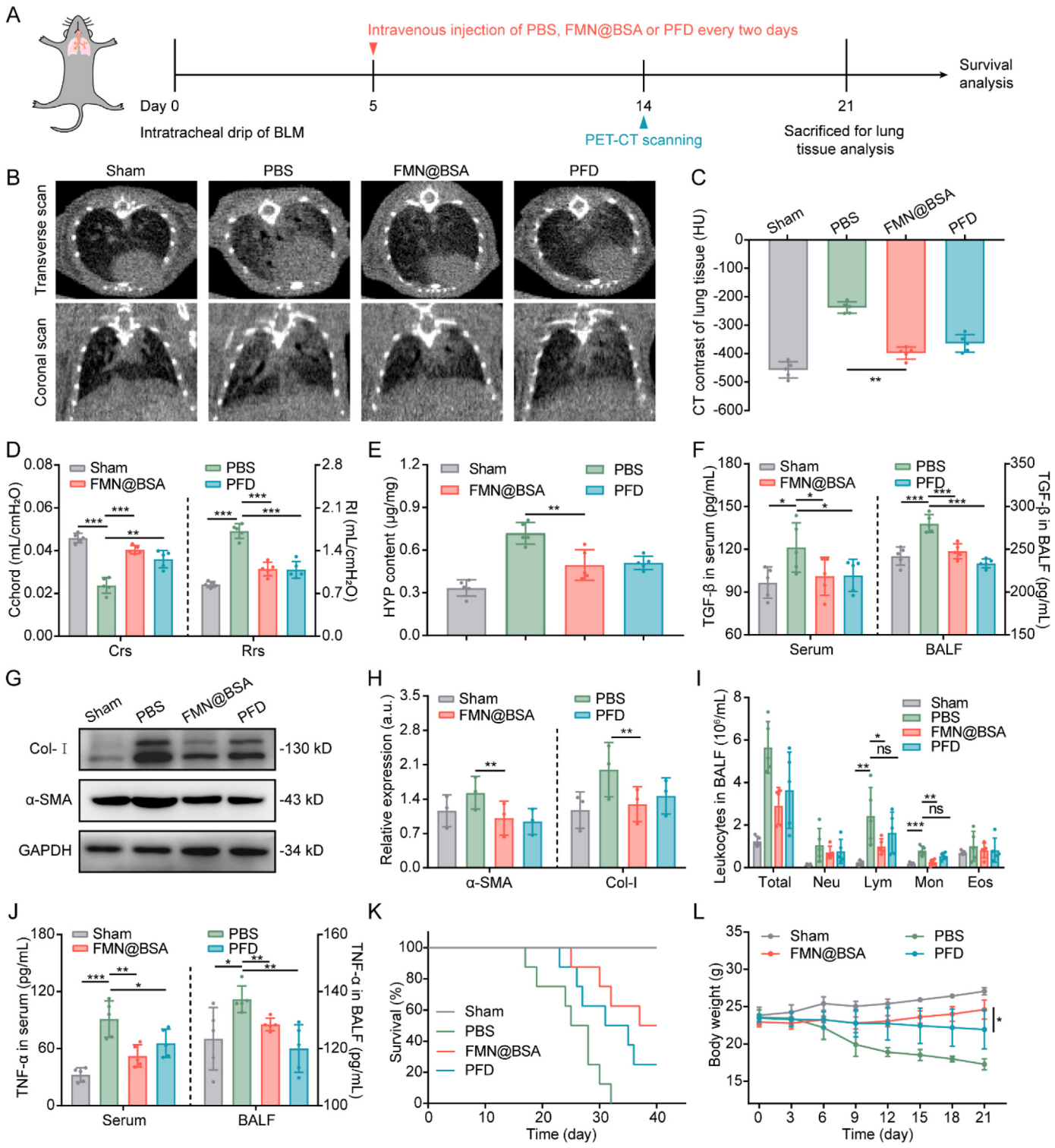

Fig. 6. *In vivo* anti-lung injury and fibrosis effects of FMN@BSA NPs. A) Schedule and timeline for treatments with various drug formulations. B) Representative transverse (top row) and coronal (bottom row) micro-CT scan images of the lungs in living mice. C) CT values of the lungs. Data were represented as mean ± SD (n = 5). D) Quantitative indices of lung function. Data were represented as mean ± SD (n = 5). E) HYP content of lung tissue collected from BLM-treated mice after the indicated treatments. Data were represented as mean ± SD (n = 5). F) TGF-β levels in serum and BALF collected from BLM-treated mice after the indicated treatments. Data were represented as mean ± SD (n = 5). G, H) Expression of α-SMA and Col-I in lung tissues collected from BLM-treated mice after the indicated treatments. Data were represented as mean ± SD (n = 3). I) Number of inflammatory cells in BALF collected from BLM-treated mice after the indicated treatments. Data were represented as mean ± SD (n = 5). J) TNF-α levels in serum and BALF collected from BLM-treated mice after the indicated treatments. Data were represented as mean ± SD (n = 5). K) Kaplan-Meier survival curve of BLM-treated mice after the indicated therapies (n = 8). L) Body weight changes of BLM-treated mice after the indicated treatments during the therapeutic period. Data were represented as mean ± SD (n = 5).

activation by inhibiting lipid accumulation. Collectively, we verified the pathogenic pathways associated with macrophage pyroptosis by combining multi-omics analysis and explored the roles of FMN@BSA NPs in the regulation of lipid metabolism to rescue pyroptotic macrophages.

3.6. The therapeutic effects of FMN@BSA NPs on lung injury and fibrosis

FMN@BSA NPs as promising inhibitors of macrophage pyroptosis motivated us to further assess the therapeutic effects of FMN@BSA NPs on BLM-induced murine lung injury and fibrosis models. The mice were divided randomly into four groups (n = 13), and *i.v.* injected with PBS, the therapeutic drug FMN@BSA NPs (10 mg/kg FMN), or the positive drug PFD (50 mg/kg) every other day (Fig. 6A). The corresponding samples were collected from five of each group on day 21, and the remaining mice observed for survival. Mice intratracheal drip of PBS as the sham-operated group. We determined the inflammation and fibrosis progression in lung tissues on day 14 through CT imaging. Especially, according to the micro-CT scan images, a range of phenomena, including the increased density of lung parenchymal region, thickening interstitial septa and bronchial walls, and localized honeycomb reticular structures, indicated the severe inflammatory and fibrotic status in lung tissue of the BLM-treated mice (Fig. 6B). In contrast, murine lung injury models treated with FMN@BSA NPs and PFD presented significantly reduced high-density shadow in the lungs, and the decreased CT values of FMN@BSA NPs also demonstrated the alleviation of lung inflammation and fibrosis (Fig. 6C).

Based on the improvement observed by CT imaging, we test the lung function of lung injury and fibrosis mice on day 21 after various treatments. As indicated by lung compliance (Crs) and airway resistance (Rrs), forced vital capacity (FVC), peak expiratory flow (PEF), forced expiratory volume in 50 ms (FEV50), and dynamic compliance (Cdyn) [47], treatments with FMN@BSA NPs or PFD were able to significantly restore the lung function of the murine lung injury and fibrosis model (Fig. 6D, S19). Then, the fresh lung tissues of these mice were collected to evaluate the corresponding fibrosis status. Hydroxyproline (HYP) serves as an important indicator to evaluate fibrosis progression and collagen deposition [48]. As shown in Fig. 6E, BLM-treated mice showed 2-fold higher HYP content in lung tissues than that in the sham-operated mice. Consistent with the amelioration in lung function, FMN@BSA NPs administration could efficiently reduce the HYP level, which was comparable to PFD treatment. Besides, we also find that TGF-β, another commonly used indicator to reveal the fibrotic process, was significantly downregulated in both serum and BALF by the nanoparticle (Fig. 6F). Furthermore, through testing fibrosis-related proteins in lung tissues, it was found that FMN@BSA NPs potently inhibited the protein expression of α-SMA and Col-I (Fig. 6G and H), indicating that FMN@BSA NPs treatment could reduce the activation of myofibroblasts, decrease collagen deposition, and effectively retard the progression of PF. Collectively, FMN@BSA NPs were conducive to relieving fibrosis and restoring lung function. Furthermore, we counted the number of total inflammatory cells, lymphocytes (Lym), monocytes (Mon), neutrophils (Neu), and eosinophils (Eos) in BALF and found that FMN@BSA NPs could return the elevation of these cells in BLM-treated mice to the normal levels (Fig. 6I). Consistently, the concentrations of TNF-α in serum and BALF collected from BLM-treated mice were also dramatically suppressed after FMN@BSA NPs treatment (Fig. 6J). Combined with the abovementioned results, it was reasonable to propose that the treatment efficacy of FMN@BSA NPs mediated by its anti-inflammatory effects.

We determined the overall treatment efficacy among all groups by comparing the survival of the lung injury and fibrosis mice. Notably, the enhanced anti-inflammatory, anti-fibrotic effect and biosafety in the FMN@BSA NPs group conferred a significantly prolonged survival time compared to untreated lung injury mice (Fig. 6K). In contrast, mice with PFD injection just exhibited a comparatively short median survival compared to mice with FMN@BSA NPs administration. Given that impaired pulmonary function cause weight loss, the body weights of the lung injury mice were recorded during the injection period (Fig. 6L). The results demonstrated that lung injury and fibrosis would cause mice rapidly lose weight, which could be slightly retarded by the PFD administration. The overall decline in the body weight of PFD-treated mice might be ascribed to the compromised treatment efficacy as well as the inherent gastrointestinal, hepatic, and renal toxicity of this standard medication [49]. In contrast, due to the potency and *in vivo* safety, the FMN@BSA NPs could efficiently halt the decreasing tendency of lung injury and fibrosis in mice body weights. Collectively, these results indicated that FMN@BSA NPs significantly and safely improved the management of lung injury and fibrosis mice at a five-time lower dose than PFD.

4. Conclusions

In this study, we developed an actively targeting nanoparticle encapsulated pyroptosis inhibitor for lung injury and fibrosis treatment based on the hypothesis that blocking the inflammatory death of alveolar macrophages could efficiently mitigate the local inflammation reaction and reduce the activation of fibroblasts to relieve fibrotic progression. FMN was tapped as a potential macrophage pyroptosis inhibitor by blocking the NLRP3 inflammasome pathway and loaded into albumin-based nanoparticles by nanoprecipitation. FMN@BSA NPs improved the bioavailability of FMN through facilitating the preferential accumulation medicated by the affinity of albumin to the SPARC protein overexpressed in inflammatory and fibrotic lesions. Upon arrival to diseased sites, FMN@BSA NPs release the cargos to block NLPR3 inflammasome activation and disrupt the pyroptotic process through regulating lipid metabolism after internalization in alveolar macrophages, leading to the downregulation of proinflammatory cytokines along with deactivation of fibroblasts. As a result, FMN@BSA NPs restored lung function and prolonged animal survival in the BLM-induced murine lung injury and fibrosis model.

Compared with Z-VAD-FMK and PFD, FMN@BSA NPs not only have favorable therapeutic effects but also have better biosafety profiles. As a nanomedicine, FMN@BSA NPs can achieve preferential drug accumulation through dual targeting by passive efflux and active binding. In contrast, small molecule drugs have a short circulation time *in vivo*, causing off-target effects that can reduce drug efficacy [50]. FMN@BSA NPs select natural products as active ingredients with low toxicity, while Z-VAD-FMK is a pan-caspase inhibitor with a high risk of toxicity, and PFD has significant gastrointestinal toxicity in clinical application [4]. Due to this, by virtue of the delivery system, the dose of FMN@BSA NPs is much lower than first-line treatment PFD, which has a much stronger clinical translation capability. Of course, there are some limitations to our study. First, FMN@BSA NPs were found to inhibit NLRP3 activation by modulating lipid metabolism in macrophages through multi-omics analyses, and preliminary *in vitro* validation was performed, but the detailed mechanism needs to be further explored. In addition, FMN@BSA NPs, while having better efficacy than PFD, did not significantly break the common survival problem. We will try a more optimal drug regimen or combination therapy to address this refractory disease in the future.

In summary, this study first employed an albumin-based nanoparticle to actively deliver the pyroptosis inhibitor to injured pulmonary tissues, which validated the involvement of macrophage pyroptosis in the pathological mechanism. Moreover, this nanomedicine would provide a promising strategy for the treatment of lung injury and fibrosis like the sequela induced by SARS-CoV-2-mediated pneumonia.

Author contributions

Boshu Ouyang and Lingling Deng conducted the experiments and wrote the manuscript with equal contribution. Fangyong Yang and Hanlin Shi provided equipment and technical support. Na Wang, Weifeng Tang, Xi Huang, Yaolong Zhou and Hang Yu took part in the *in vivo* experiments. The manuscript was written through contributions of all

authors. Ying Wei helped analyze the data and revise the manuscript. Jingcheng Dong completed the conceptualization and methodology of the article. All authors have given approval to the final version of the manuscript.

Declaration of competing interest

The authors declare that they have no known competing financial interests or personal relationships that could have appeared to influence the work reported in this paper.

Data availability

No data was used for the research described in the article.

Acknowledgments

This work was supported by the Foundation of Shanghai Science and Technology Commission (Grant No.YDZX00003008, No.22DZ2292000), the original research project of Fudan University (Grant No. 202101) and innovative research team of high-level local universities in Shanghai-Clinical and basic research on the prevention and treatment of some inflammatory diseases by integrative medicine. The authors deeply thank Yawen Song and the teamwork (Oebiotech Co., Ltd., Shanghai, China) for proteomics and metabolomics characterization. The authors also thank Shiyanjia Lab (www.shiyanjia.com) for TEM and SEM analysis.

Appendix A. Supplementary data

Supplementary data to this article can be found online at https://doi.org/10.1016/j.mtbio.2023.100643.

References

[1] C.E. Rubenfeld Gd, E. Peabody, J. Weaver, D.P. Martin, M. Neff, E.J. Stern, L.D. Hudson, Incidence and outcomes of acute lung injury, N. Engl. J. Med. 353 (16) (2005) 1685–1693.
[2] N. Clementi, S. Ghosh, M. De Santis, M. Castelli, E. Criscuolo, I. Zanoni, M. Clementi, N. Mancini, Viral respiratory pathogens and lung injury, Clin. Microbiol. Rev. 34 (3) (2021).
[3] T.A. Wynn, T.R. Ramalingam, Mechanisms of fibrosis: therapeutic translation for fibrotic disease, Nat. Med. 18 (7) (2012) 1028–1040.
[4] D.J. Lederer, F.J. Martinez, Idiopathic pulmonary fibrosis, N. Engl. J. Med. 378 (19) (2018) 1811–1823.
[5] L. Wollin, E. Wex, A. Pautsch, G. Schnapp, K.E. Hostettler, S. Stowasser, M. Kolb, Mode of action of nintedanib in the treatment of idiopathic pulmonary fibrosis, Eur. Respir. J. 45 (5) (2015) 1434–1445.
[6] P. Cheng, S. Li, H. Chen, Macrophages in lung injury, repair, and fibrosis, Cells 10 (2) (2021) 436.
[7] I. Lasithiotaki, I. Giannarakis, E. Tsitoura, K.D. Samara, G.A. Margaritopoulos, C. Choulaki, E. Vasarmidi, N. Tzanakis, A. Voloudaki, P. Sidiropoulos, N.M. Siafakas, K.M. Antoniou, NLRP3 inflammasome expression in idiopathic pulmonary fibrosis and rheumatoid lung, Eur. Respir. J. 47 (3) (2016) 910–918.
[8] C. Junqueira, A. Crespo, S. Ranjbar, L.B. de Lacerda, M. Lewandrowski, J. Ingber, B. Parry, S. Ravid, S. Clark, M.R. Schrimpf, F. Ho, C. Beakes, J. Margolin, N. Russell, K. Kays, J. Boucau, U. Das Adhikari, S.M. Vora, V. Leger, L. Gehrke, L. Henderson, E. Janssen, D. Kwon, C. Sander, J. Abraham, M.B. Goldberg, H. Wu, G. Mehta, S. Bell, A.E. Goldfeld, M.R. Filbin, J. Lieberman, FcgammaR-mediated SARS-CoV-2 infection of monocytes activates inflammation, Nature 606 (7914) (2022) 576–584.
[9] J.W. Meiyue Song, Youliang Sun, Junling Pang, Xiaona Li, Yuan Liu, Yitian Zhou, Peiran Yang, Tianhui Fan, Ying Liu, Zhaoguo Li, Xianmei Qi, Baicun Li, Xinri Zhang, Jing Wang, Chen Wang, Inhibition of gasdermin D-dependent pyroptosis attenuates the progression of silicainduced pulmonary inflammation and fibrosis, APSB 12 (3) (2022) 1213–1224.
[10] Z. Song, Q. Gong, J. Guo, Pyroptosis: mechanisms and links with fibrosis, Cells 10 (12) (2021) 3509.
[11] S.P. Newman, Delivering drugs to the lungs: the history of repurposing in the treatment of respiratory diseases, Adv. Drug Deliv. Rev. 133 (2018) 5–18.
[12] R. Brusini, M. Varna, P. Couvreur, Advanced nanomedicines for the treatment of inflammatory diseases, Adv. Drug Deliv. Rev. 157 (2020) 161–178.
[13] L. Sun, Y. Liu, X. Liu, R. Wang, J. Gong, A. Saferali, W. Gao, A. Ma, H. Ma, S.E. Turvey, S.Y. Fung, H. Yang, Nano-enabled reposition of proton pump inhibitors for tlr inhibition: toward A new targeted nanotherapy for acute lung injury, Adv. Sci. 9 (3) (2022), e2104051.
[14] T. Tian, T. Zhang, S. Shi, Y. Gao, X. Cai, Y. Lin, A dynamic DNA tetrahedron framework for active targeting, Nat. Protoc. 18 (4) (2023) 1028–1055.
[15] D. Frank, J.E. Vince, Pyroptosis versus necroptosis: similarities, differences, and crosstalk, Cell Death Differ. 26 (1) (2019) 99–114.
[16] A. Wree, A. Eguchi, M.D. McGeough, C.A. Pena, C.D. Johnson, A. Canbay, H.M. Hoffman, A.E. Feldstein, NLRP3 inflammasome activation results in hepatocyte pyroptosis, liver inflammation, and fibrosis in mice, Hepatology 59 (3) (2014) 898–910.
[17] Y. Chen, R. Luo, J. Li, S. Wang, J. Ding, K. Zhao, B. Lu, W. Zhou, Intrinsic radical species scavenging activities of tea polyphenols nanoparticles block pyroptosis in endotoxin-induced sepsis, ACS Nano 16 (2) (2022) 2429–2441.
[18] Y. Jiang, S. Li, T. Zhang, M. Zhang, Y. Chen, Y. Wu, Y. Liu, Z. Liu, Y. Lin, Tetrahedral framework nucleic acids inhibit skin fibrosis via the pyroptosis pathway, ACS Appl. Mater. Interfac. 14 (13) (2022) 15069–15079.
[19] T.L. Désogère P, L.P. Hariri, N.J. Rotile, T.A. Rietz, C.K. Probst, F. Blasi, H. Day, M. Mino-Kenudson, P. Weinreb, S.M. Violette, B.C. Fuchs, A.M. Tager, M. Lanuti, P. Caravan, Type I collagen–targeted PET probe for pulmonary fibrosis detection and staging in preclinical models, Sci. Transl. Med. 9 (384) (2017) 4696.
[20] P. Bornstein, Diversity of function is inherent in matricellular proteins: an appraisal of thrombospondin 1, J. Cell Biol. 130 (1995) 503–506.
[21] Z.Z. Savani Rc, E. Arguiri, S. Wang, D. Vu, C.C. Howe, H.M. DeLisser, Bleomycin-induced pulmonary injury in mice deficient in SPARC, Am. J. Physiol. Lung Cell Mol. Physiol. 279 (4) (2000) L743–L750.
[22] L. Liu, F. Hu, H. Wang, X. Wu, A.S. Eltahan, S. Stanford, N. Bottini, H. Xiao, M. Bottini, W. Guo, X.-J. Liang, Secreted protein acidic and rich in cysteine mediated biomimetic delivery of methotrexate by albumin-based nanomedicines for rheumatoid arthritis therapy, ACS Nano 13 (5) (2019) 5036–5048.
[23] Y. Zhang, C. Mao, Y. Zhan, Y. Zhao, Y. Chen, Y. Lin, Albumin-coated framework nucleic acids as bionic delivery system for triple-negative breast cancer therapy, ACS Appl. Mater. Interfac. 14 (35) (2022) 39819–39829.
[24] T. Tian, Y. Li, Y. Lin, Prospects and challenges of dynamic DNA nanostructures in biomedical applications, Bone Research 10 (1) (2022).
[25] E.N. Hoogenboezem, C.L. Duvall, Harnessing albumin as a carrier for cancer therapies, Adv. Drug Deliv. Rev. 130 (2018) 73–89.
[26] L. Yi, J. Cui, W. Wang, W. Tang, F. Teng, X. Zhu, J. Qin, T. Wuniqiemu, J. Sun, Y. Wei, J. Dong, Formononetin attenuates airway inflammation and oxidative stress in murine allergic asthma, Front. Pharmacol. 11 (2020), 533841.
[27] D. Wu, K. Wu, Q. Zhu, W. Xiao, Q. Shan, Z. Yan, J. Wu, B. Deng, Y. Xue, W. Gong, G. Lu, Y. Ding, Formononetin administration ameliorates dextran sulfate sodium-induced acute colitis by inhibiting NLRP3 inflammasome signaling pathway, Mediat. Inflamm. 2018 (2018), 3048532.
[28] L.Y. Luo, M.X. Fan, H.Y. Zhao, M.X. Li, X. Wu, W.Y. Gao, Pharmacokinetics and bioavailability of the isoflavones formononetin and ononin and their in vitro absorption in ussing chamber and caco-2 cell models, J. Agric. Food Chem. 66 (11) (2018) 2917–2924.
[29] H. Xian, Y. Liu, A. Rundberg Nilsson, R. Gatchalian, T.R. Crother, W.G. Tourtellotte, Y. Zhang, G.R. Aleman-Muench, G. Lewis, W. Chen, S. Kang, M. Luevanos, D. Trudler, S.A. Lipton, P. Soroosh, J. Teijaro, J.C. de la Torre, M. Arditi, M. Karin, E. Sanchez-Lopez, Metformin inhibition of mitochondrial ATP and DNA synthesis abrogates NLRP3 inflammasome activation and pulmonary inflammation, Immunity 54 (7) (2021) 1463–1477.
[30] Q. Chen, X. Liu, J. Chen, J. Zeng, Z. Cheng, Z. Liu, A self-assembled albumin-based nanoprobe for in vivo ratiometric photoacoustic pH imaging, Adv. Mater. 27 (43) (2015) 6820–6827.
[31] N.A.E.S. V Szapiel, J.D. Fulmer, G.W. Hunninghake, R.G. Crystal, Bleomycin-induced interstitial pulmonary disease in the nude, athymic mouse, Am. Rev. Respir. Dis. 120 (4) (1979) 893–899.
[32] J.M.S. T Ashcroft, V. Timbrell, Simple method of estimating severity of pulmonary fibrosis on a numerical scale, J. Clin. Pathol. 41 (4) (1988) 467–470.
[33] C. Yu, Z. Chen, X. Li, H. Bao, Y. Wang, B. Zhang, J. Huang, Z. Zhang, pH-triggered aggregation of gold nanoparticles for enhanced labeling and long-term CT imaging tracking of stem cells in pulmonary fibrosis treatment, Small 17 (33) (2021), 2101861.
[34] X. Chen, W.T. He, L. Hu, J. Li, Y. Fang, X. Wang, X. Xu, Z. Wang, K. Huang, J. Han, Pyroptosis is driven by non-selective gasdermin-D pore and its morphology is different from MLKL channel-mediated necroptosis, Cell Res. 26 (9) (2016) 1007–1020.
[35] X. Ma, J. Hao, J. Wu, Y. Li, X. Cai, Y. Zheng, Prussian blue nanozyme as a pyroptosis inhibitor alleviates neurodegeneration, Adv. Mater. (2022), e2106723.
[36] G.R. Grotendorst, H. Rahmanie, M.R. Duncan, Combinatorial signaling pathways determine fibroblast proliferation and myofibroblast differentiation, Faseb. J. 18 (3) (2004) 469–479.
[37] X.L. Chang X, Y. Wang, C.X. Yang, Y.J. He, T.J. Zhou, X.D. Gao, L. Li, H.P. Hao, H.L. Jiang, Monocyte-derived multipotent cell delivered programmed therapeutics to reverse idiopathic pulmonary fibrosis, Sci. Adv. 6 (22) (2020), eaba3167.
[38] J. Wu, D. Song, Z. Li, B. Guo, Y. Xiao, W. Liu, L. Liang, C. Feng, T. Gao, Y. Chen, Y. Li, Z. Wang, J. Wen, S. Yang, P. Liu, L. Wang, Y. Wang, L. Peng, G.N. Stacey, Z. Hu, G. Feng, W. Li, Y. Huo, R. Jin, N. Shyh-Chang, Q. Zhou, L. Wang, B. Hu, H. Dai, J. Hao, Immunity-and-matrix-regulatory cells derived from human embryonic stem cells safely and effectively treat mouse lung injury and fibrosis, Cell Res. 30 (9) (2020) 794–809.
[39] A. Moeller, K. Ask, D. Warburton, J. Gauldie, M. Kolb, The bleomycin animal model: a useful tool to investigate treatment options for idiopathic pulmonary fibrosis? Int. J. Biochem. Cell Biol. 40 (3) (2008) 362–382.
[40] Y. Wang, X. Zhou, K. Zou, G. Chen, L. Huang, F. Yang, W. Pan, H. Xu, Z. Xu, H. Chen, J. Chen, S. Gong, X. Zhou, W. Xu, J. Zhao, Monocarboxylate transporter 4 triggered cell pyroptosis to aggravate intestinal inflammation in inflammatory bowel disease, Front. Immunol. 12 (2021), 644862.

[41] X. Zhao, J.Y.Y. Kwan, K. Yip, P.P. Liu, F.-F. Liu, Targeting metabolic dysregulation for fibrosis therapy, Nat. Rev. Drug Discov. 19 (1) (2020) 57–75.
[42] D. Tang, R. Kang, T.V. Berghe, P. Vandenabeele, G. Kroemer, The molecular machinery of regulated cell death, Cell Res. 29 (5) (2019) 347–364.
[43] W. Huang da, B.T. Sherman, R.A. Lempicki, Systematic and integrative analysis of large gene lists using DAVID bioinformatics resources, Nat. Protoc. 4 (1) (2009) 44–57.
[44] P.K. Anand, Lipids, inflammasomes, metabolism, and disease, Immunol. Rev. 297 (1) (2020) 108–122.
[45] S.S. Im, L. Yousef, C. Blaschitz, J.Z. Liu, R.A. Edwards, S.G. Young, M. Raffatellu, T.F. Osborne, Linking lipid metabolism to the innate immune response in macrophages through sterol regulatory element binding protein-1a, Cell Metabol. 13 (5) (2011) 540–549.
[46] M.P. Wymann, R. Schneiter, Lipid signalling in disease, Nat. Rev. Mol. Cell Biol. 9 (2) (2008) 162–176.
[47] P.C. Dinh, D. Paudel, H. Brochu, K.D. Popowski, M.C. Gracieux, J. Cores, K. Huang, M.T. Hensley, E. Harrell, A.C. Vandergriff, A.K. George, R.T. Barrio, S. Hu, T.A. Allen, K. Blackburn, T.G. Caranasos, X. Peng, L.V. Schnabel, K.B. Adler, L.J. Lobo, M.B. Goshe, K. Cheng, Inhalation of lung spheroid cell secretome and exosomes promotes lung repair in pulmonary fibrosis, Nat. Commun. 11 (1) (2020) 1064.
[48] K.P. Srivastava Ak, H.K. Nagar, N. Raghuwanshi, R. Srivastava, Hydroxyproline: a potential biochemical marker and its role in the pathogenesis of different diseases, Curr. Protein Pept. Sci. 17 (2016) 596–602, 1875-5550 (Electronic)).
[49] L. Richeldi, H.R. Collard, M.G. Jones, Idiopathic pulmonary fibrosis, Lancet 389 (10082) (2017) 1941–1952.
[50] C.G. Da Silva, F. Rueda, C.W. Lowik, F. Ossendorp, L.J. Cruz, Combinatorial prospects of nano-targeted chemoimmunotherapy, Biomaterials 83 (2016) 308–320.